nature biomedical engineering

ARTICLES

https://doi.org/10.1038/s41551-019-0501-5

Cytosine and adenine base editing of the brain, liver, retina, heart and skeletal muscle of mice via adeno-associated viruses

Jonathan M. Levy[1,2,3], Wei-Hsi Yeh[1,2,3,4], Nachiket Pendse[5,6], Jessie R. Davis[1,2,3], Erin Hennessey[5,6], Rossano Butcher[5,6], Luke W. Koblan[1,2,3], Jason Comander[5,6], Qin Liu[5,6] and David R. Liu[1,2,3]*

The success of base editors for the study and treatment of genetic diseases depends on the ability to deliver them in vivo to the relevant cell types. Delivery via adeno-associated viruses (AAVs) is limited by AAV packaging capacity, which precludes the use of full-length base editors. Here, we report the application of dual AAVs for the delivery of split cytosine and adenine base editors that are then reconstituted by *trans*-splicing inteins. Optimized dual AAVs enable in vivo base editing at therapeutically relevant efficiencies and dosages in the mouse brain (up to 59% of unsorted cortical tissue), liver (38%), retina (38%), heart (20%) and skeletal muscle (9%). We also show that base editing corrects, in mouse brain tissue, a mutation that causes Niemann–Pick disease type C (a neurodegenerative ataxia), slowing down neurodegeneration and increasing lifespan. The optimized delivery vectors should facilitate the efficient introduction of targeted point mutations into multiple tissues of therapeutic interest.

Point mutations represent the majority of known pathogenic human genetic variants[1]. To enable the direct installation or correction of point mutations in living cells, we developed base editors—engineered proteins that directly convert a target base pair to a different base pair without creating double-stranded DNA breaks[2–4]. Cytosine base editors (CBEs) such as BE4max[3,5–7] catalyse the conversion of target C•G base pairs to T•A, while adenine base editors (ABEs) such as ABEmax[4,6] convert target A•T base pairs to G•C. While CBEs and ABEs are both widely used and work robustly in many cultured mammalian cell systems[2], the efficient delivery of base editors into live animals remains a challenge, despite promising initial studies[8–10]. A major impediment to the delivery of base editors in animals has been an inability to package base editors in adeno-associated virus (AAV)—an efficient and widely used delivery agent that remains the only Food and Drug Administration-approved in vivo gene therapy vector[11]. The large size of the DNA encoding base editors (5.2 kilobases (kb) for base editors containing *Streptococcus pyogenes* Cas9, not including any guide RNA or regulatory sequences) precludes packaging in AAV, which has a genome packaging size limit of ≤5 kb (refs. [12,13]).

To bypass this packaging size limit and deliver base editors using AAVs, we devised a split base-editor dual-AAV strategy[14,15] in which the CBE or ABE is divided into an amino-terminal and carboxy-terminal half. Each base-editor half is fused to half of a fast-splicing split intein. Following co-infection by AAV particles expressing each base editor–split-intein half, protein splicing in *trans* reconstitutes full-length base editor. Unlike other approaches utilizing small molecules[16] or single guide RNA (sgRNA)[17] to bridge split Cas9, intein splicing removes all exogenous sequences and regenerates a native peptide bond at the split site, resulting in a single reconstituted protein identical in sequence to the unmodified base editor.

In this study, we developed split-intein CBEs and split-intein ABEs, and integrated them into optimized dual-AAV genomes that enable the most efficient base editing to date in somatic tissues of therapeutic relevance, including liver, heart, muscle, retina and brain. We used the resulting AAVs to achieve base-editing efficiencies at test loci for both CBEs and ABEs that, in each of these tissues, meet or exceed therapeutically relevant editing thresholds for the treatment of some human genetic diseases at AAV dosages that are known to be well tolerated in humans. Integrating these developments, we used dual-AAV split-intein base editors to treat a mouse model of Niemann–Pick disease type C (NPC)—a debilitating disease that affects the central nervous system (CNS), resulting in correction of the casual mutation in CNS tissue, preservation of target neurons and an increase in animal lifespan.

Results

Development of a split-intein approach to CBE and ABE reconstitution. We reasoned that the use of a *trans*-splicing intein would enable CBE and ABE to be divided into halves that are each smaller than the AAV packaging size limit, enabling dual-AAV packaging of base editors (Fig. 1a). To generate a split-intein CBE, we first fused each split DnaE intein half from *Nostoc punctiforme* (Npu)[18] to each half of the original CBE BE3 (ref. [3])—a fusion protein of rat apolipoprotein B messenger RNA (mRNA) editing enzyme, catalytic polypeptide 1 (APOBEC1), *S. pyogenes* Cas9 and uracil glycosylase inhibitor (UGI) from bacteriophage PBS1, dividing BE3 within the *S. pyogenes* Cas9 domain[15,19] immediately before Cys 574 or Thr 638. We observed that dividing BE3 just before Cys 574 with the split Npu intein (referred to hereafter as the Npu-BE3 construct) resulted in robust on-target base editing (34 ± 6.4% average editing by high-throughput sequencing among unsorted cells targeting six

[1]Merkin Institute of Transformative Technologies in Healthcare, Broad Institute of Harvard and MIT, Cambridge, MA, USA. [2]Department of Chemistry and Chemical Biology, Harvard University, Cambridge, MA, USA. [3]Howard Hughes Medical Institute, Harvard University, Cambridge, MA, USA. [4]Program in Speech and Hearing Bioscience and Technology, Harvard Medical School, Boston, MA, USA. [5]Ocular Genomics Institute, Massachusetts Eye and Ear Institute, Boston, MA, USA. [6]Department of Ophthalmology, Harvard Medical School, Boston, MA, USA. *e-mail: drliu@fas.harvard.edu

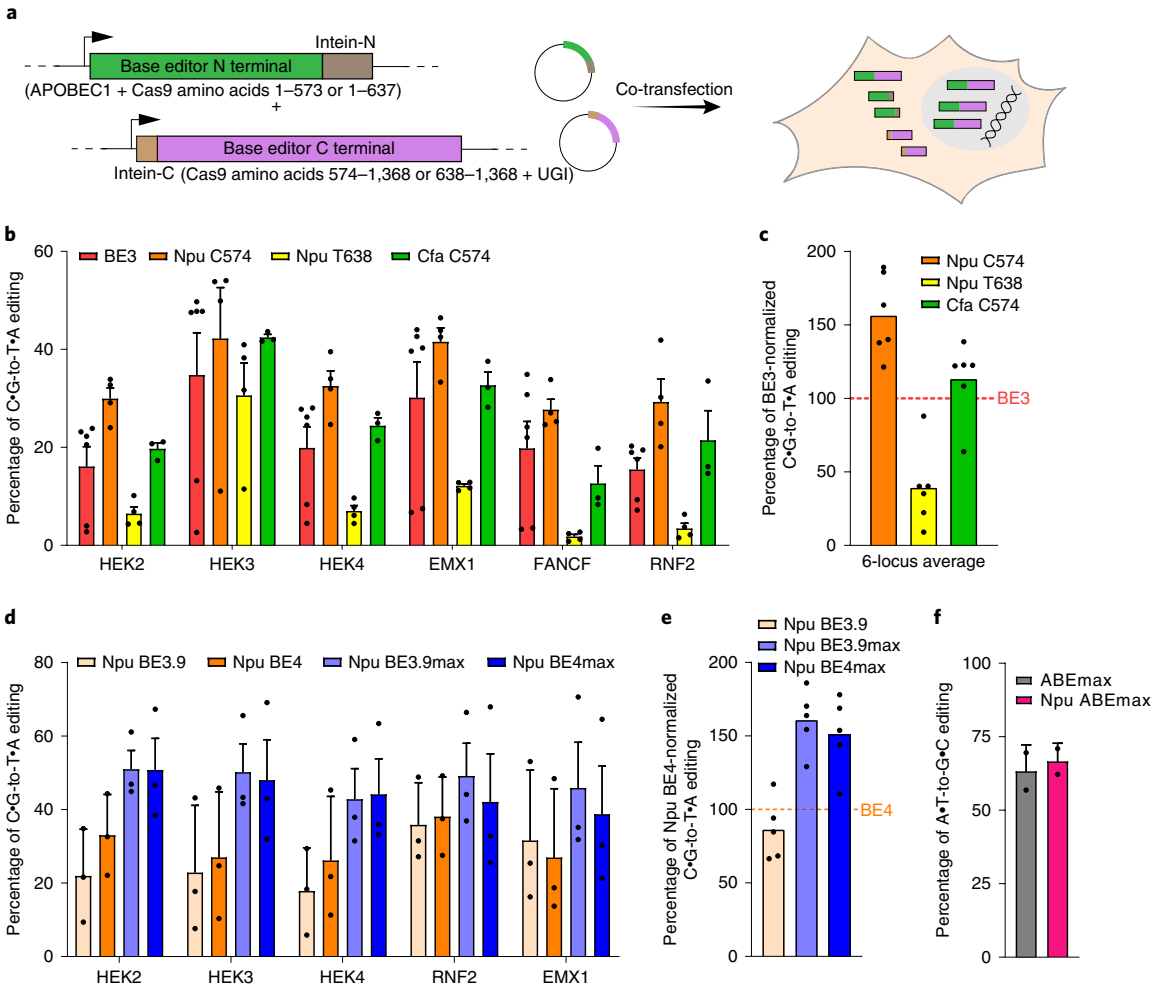

Fig. 1 | Development of split-intein CBEs and ABEs. a, Intein reconstitution strategy. Two separately encoded protein fragments fused to split-intein halves splice to reconstitute full-length protein following co-expression. C, carboxy terminal; N, amino terminal. **b**, Lipofection of intact BE3 (red), split BE3 with the Npu split-intein site between E573 and C574 (orange) or K637 and T638 (yellow), or split BE3 with the Cfa split-intein site between E573 and C574 (green) into HEK293T cells, followed by high-throughput sequencing of six test loci to determine base-editing efficiency. **c**, Comparison of the six-loci averages for the editing data in **b**, normalized to BE3 levels (dotted line). BE3-normalized editing at each locus (black dots) was averaged. **d**, 'BEmax' optimization of NLSs and codon usage increases the editing efficiency at five standard loci. BE3.9max and BE4max show comparable editing efficiencies. **e**, Comparison of the five-loci averages for the editing data in **d**, normalized to BE4 levels (dotted line). **f**, Lipofection of ABEmax or Npu split E573/C574 ABEmax into NIH 3T3 cells for the generation of a split-intein adenosine base editor. The editing data are for the *DNMT1* locus. In **b**, **d** and **f**, dots represent values and bars represent mean + s.d. of $n = 3$ (**b** and **d**) or $n = 2$ (**f**) independent biological replicates (see Methods for details). Dots in **c** and **e** represent locus averages.

genomic loci; Fig. 1b) in HEK293T cells following co-transfection of plasmids expressing each split half, plus a third plasmid expressing sgRNA. Notably, target C•G-to-T•A editing efficiency was higher, rather than lower, than editing levels following transfection of a plasmid expressing an intact BE3, which resulted in an average of 22 ± 7.9% editing across the six sites (Fig. 1b,c), indicating that intein splicing at Cys 574 does not limit the editing efficiency in this system. We speculate that higher expression levels of each split-intein base-editor half, relative to that of the much larger intact base-editor proteins, may account for increased editing from split-intein base editors. Interestingly, the second tested BE3 split site, ahead of Thr 638, did not support robust base editing (averaging 10 ± 10% editing across six sites) even though both split sites support Cas9 nuclease activity[15], suggesting that base editors impose additional requirements for productive intein splicing or productive editing compared with Cas9 nuclease.

After identifying a BE3 split site that does not impair base-editing efficiency following intein splicing, we next optimized split-intein CBE performance. We compared the performance of the Npu split intein with that of Cfa—a synthetic split intein developed from the consensus sequences of fast-splicing DnaE homologues from a variety of organisms[20]. Npu-BE3 outperformed Cfa-BE3, which resulted in 25 ± 10% average base editing (Fig. 1b,c). To incorporate recent architectural improvements in our newer BE4 base editor[5], as well as improved expression and nuclear localization of BE4max[6], we generated Npu-BE4 constructs and tested two codon usages. Consistent with our recent report[6], we observed that codon and nuclear localization signal (NLS) optimization of Npu-BE4max resulted in higher base-editing efficiencies than Npu-BE4 using IDT codon optimization (44 ± 4.2% editing versus 26 ± 3.0% editing; Fig. 1d). We also found that the second UGI domain, which improves C•G-to-T•A editing outcomes in some architectures[5], did not increase the editing efficiency of Npu-BE4max; a single UGI in the BEmax architecture yields 48 ± 3.0% editing (Fig. 1d,e). In light of these results, we omitted the second UGI from future AAV constructs to minimize the viral genome size, resulting in a spliced

NLS- and codon-optimized APOBEC–Cas9 nickase–UGI construct that we refer to hereafter as CBE3.9max.

We were intrigued by the comparable editing efficiencies of full-length and intein-split base editors. To measure relative expression levels, we performed western blots in HEK cells transfected with haemagglutinin (HA)- and FLAG-tagged split halves and an sgRNA targeting the HEK3 locus, finding that the co-expression of the split halves generates unspliced and full-length CBE3.9max (Supplementary Fig. 1d). Sequencing data show that all constructs efficiently edit the HEK3 locus (Supplementary Fig. 1e). We additionally tested an inactivating split-intein mutation, Npu C1A, that inhibits splicing following intein association[21]. Although these C1A constructs did not generate full-length CBE3.9max, they robustly edited HEK3 (Supplementary Fig. 1d,f). These data indicate that in addition to mediating covalent splicing and reconstitution of full-length base editors, the inteins are able to mediate association of the editor split halves and generate functional base editor without splicing.

We also used the Cys 574 Cas9 split site and the Npu split intein to generate a split-optimized ABEr (Npu-ABEmax) construct. To test whether Npu-ABEmax reconstitutes ABEmax[6] activity, we installed a silent mutation in the mouse *DNMT1* locus (which has been shown to be amenable to Cas9 cutting activity[22]) in 3T3 cells, finding that Npu-ABEmax and ABEmax have equal activity (63 ± 5.4% A•T-to-G•C editing from Npu-ABEmax, compared with 63 ± 6.3% editing from non-split ABEmax; Fig. 1f). Finally, we screened seven split sites in *Staphylococcus aureus* Cas9–BE3 (SaBE3)[23] and identified a site immediately before Cys 535 that fully recapitulated unsplit SaBE3 activity in HEK293T cells (Supplementary Fig. 1). A recent report showed that another intein split site, preceding Ser 740, reconstitutes full-length SaCas9 nuclease activity and supports split SaBE3 activity in vivo[24]. Together, these results establish optimized split-intein CBE and ABE halves that, upon protein splicing, reconstitute CBEs and ABEs with no apparent loss in editing efficiency.

Development of split-intein CBE and ABE AAV. After developing a viable way to divide both classes of base editors into split intein-fused halves, we generated and characterized a series of AAV particles to optimize the base-editing efficiency and minimize AAV genome size to support efficient AAV production[25]. We tested several post-transcriptional regulatory element sequences (PREs) and sgRNA positions in the context of AAV, rather than plasmid delivery, to maximize the in vivo relevance of the optimization process.

To avoid effects specific to cultured cells, we used PHP.B[26]—an evolved AAV variant that efficiently crosses the blood–brain barrier in mice—to test PRE variants in the mouse CNS. We delivered 1×10^{11} viral genomes (vg) of CMV-enhanced green fluorescent protein (EGFP)–NLS containing either no PRE, a full-length Woodchuck hepatitis virus PRE (WPRE) sequence or a truncated WPRE[27] into 8-week-old mice by retro-orbital injection, and harvested brain tissue for imaging after a 3-week incubation. W3 increased PHP.B-delivered green fluorescent protein (GFP)–NLS expression levels in the brain ~19-fold compared with no regulatory sequence (Fig. 2a–c). This increase in payload gene expression was comparable to the increase from using the full-length WPRE sequence (20-fold; Fig. 2a–c), but W3 is 350 base pairs smaller than full-length WPRE.

Although the tendency of the CMV promoter to be silenced over time in vivo may be beneficial for some genome-editing applications by minimizing off-target editing opportunities[19,28,29], we chose to avoid silencing to maximize editing efficiency in this initial study. The Cbh promoter is a ubiquitous, constitutive promoter that is less sensitive to silencing in vivo than the CMV promoter[30]. All base-editor AAV constructs therefore contained the truncated W3 sequence, Npu intein and Cbh promoter, which we refer to hereafter as v3 AAV. To optimize split base-editor AAV configurations, we transduced murine 3T3 cells with dual v3 AAV-PHP.B encoding split CBE3.9 and a validated sgRNA targeting the mouse *DNMT1* locus[22]. A dose of 2×10^{10} vg AAV total per well of 50,000 NIH 3T3 cells, using a 1:1 ratio of the two AAVs, resulted in 1.7 ± 0.73% C•G-to-T•A editing at the *DNMT1* locus. Replacing CBE3.9 with the NLS- and codon-optimized CBE3.9max to generate v4 AAV-CBE3.9max improved the C•G-to-T•A editing efficiency to 4.1 ± 2.2%—a 2.4-fold increase relative to v3 AAV-CBE3.9 (Fig. 2d,e).

After optimizing PRE, promoter, NLS and codon usage, we tested the impact of different guide RNA placements and orientations within the AAV genome. Guide RNA transcription efficiency is known to be sensitive to proximity and orientation relative to AAV inverted terminal repeats (ITRs)[31]. Moving the U6-sgRNA cassette to the 3′ end of the viral genome and reversing its orientation[31], yielding v5 AAV, improved the C•G-to-T•A editing efficiency a further 5.6-fold relative to v4 AAV, for a total 14-fold improvement compared with the initial v3 AAV constructs (23 ± 5.2% for v5 AAV-CBE3.9max versus 1.7 ± 0.73% for v3 AAV-CBE3.9). We repeated these experiments at a tenfold higher virus dose (2×10^{11} vg per well) and observed fourfold higher C•G-to-T•A editing efficiency for v5 AAV compared with v3 AAV, and 1.5-fold higher editing for v5 AAV compared with v4 AAV (14 ± 4.8% for v3 AAV-CBE3.9; 37 ± 18% for v4 AAV-CBE3.9max; and 56 ± 12% for v5 AAV-CBE3.9max) (Fig. 2d,e). Based on these results, we used CBE3.9max and ABEmax in the optimized v5 AAV architecture, referred to hereafter as v5 AAV-CBE or v5 AAV-ABE, for all of the subsequent experiments. We note that v5 AAV-ABE genomes contain an sgRNA cassette only on the carboxy-terminal half due to size constraints, while v5 AAV-CBE genomes contain sgRNA cassettes on both halves.

Next, we characterized the performance of the optimized AAV split-intein base-editor constructs in vivo. AAV9 is reported to transduce tissues including liver, skeletal muscle, heart and CNS[32–34]. We generated dual-AAV9 particles in the v5 AAV architecture encoding the optimized split CBE3.9max (Fig. 2d) or ABEmax base editors (Supplementary Fig. 2), together with a guide RNA programmed to install a point mutation in *DNMT1*, resulting in A8T for CBE3.9max, or a silent mutation for ABEmax. Importantly, removal of the amino-terminal 290 amino acids of DNMT1 has been shown to have minimal functional impact[35], and *DNMT1* itself acts redundantly with *DNMT3a* in the mammalian brain[36]. We therefore do not anticipate *DNMT1* base editing to incur a fitness penalty. We performed systemic (retro-orbital) injections of v5 AAV9-CBE or v5 AAV9-ABE in 6- to 9-week-old C57BL/6 mice. Four weeks after injection of 2×10^{12} vg total per mouse, we measured *DNMT1* editing in the heart, skeletal muscle, brain, liver, lung, kidney, spleen and reproductive organs. Following a single dual-AAV injection, both split-intein ABE and CBE AAVs resulted in substantial whole-organ base editing of heart (CBE: 15 ± 3.8% C•G-to-T•A editing efficiency in unsorted cells; ABE: 20 ± 1.4% A•T-to-G•C editing efficiency in unsorted cells), skeletal muscle (CBE: 4.4 ± 2.4%; ABE: 9.2 ± 4.0%) and liver (CBE: 21 ± 17%; ABE: 38 ± 2.9%) (Fig. 3a,b)—three organs that are reported to be transduced by AAV9. Consistent with the previously reported intravenous transduction profile of AAV9 (ref. [37]), we saw little editing in lung, kidney, spleen and reproductive organs, and no detectable editing in harvested sperm (Supplementary Fig. 3). Together, these results establish that AAV9 delivery of split-intein CBE and ABE enables efficient in vivo base editing in tissues known to be transduced by AAV9.

In a recent study, Kim and coworkers[8] reported AAV-mediated delivery of ABE split by *trans*-mRNA splicing. To directly compare the efficiency of AAV-delivered base editors reconstituted through split-intein-mediated splicing, versus *trans*-mRNA splicing, we generated *trans*-mRNA splicing constructs with the *DNMT1*-targeting

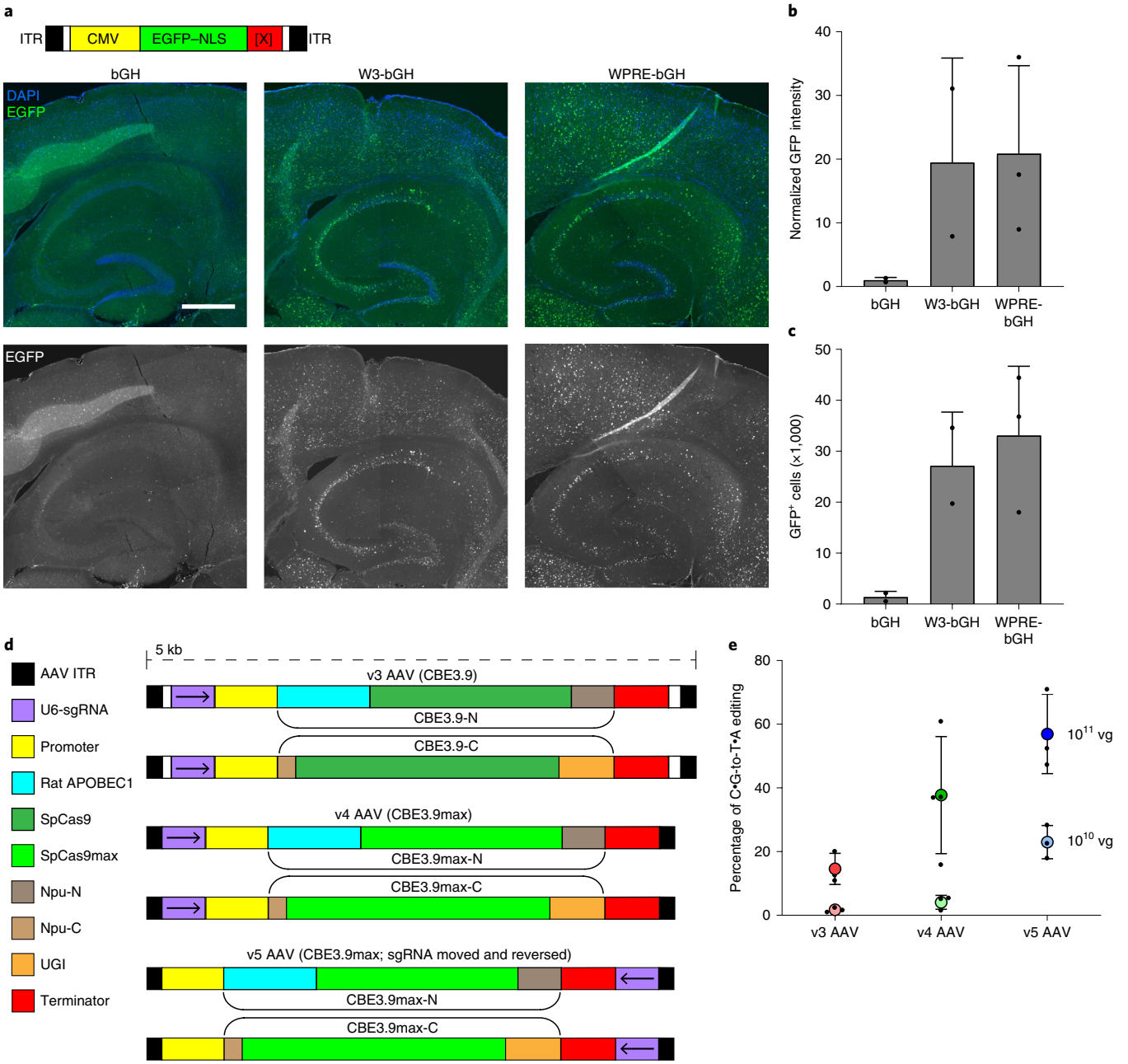

Fig. 2 | Optimization of split-intein base-editor AAVs. a, GFP expression 3 weeks after injection of 1×10^{11} vg GFP–NLS-bGH ($n=2$ mice; $n=12$ images), GFP–NLS-W3-bGH ($n=3$ mice; $n=18$ images) or GFP–NLS-WPRE-bGH ($n=2$ mice; $n=18$ images) into 6-week-old C57BL/6 mice. Representative images of horizontal brain slices show hippocampus and neocortex. Top: DAPI and EGFP signals overlaid. Bottom: EGFP signal only. Scale bar, 500 μm. **b**, Transcriptional regulatory element optimization. Total GFP signal was measured using ImageJ from the mice described in **a** (see the Methods for a detailed description of the imaging and analysis procedures). **c**, Number of GFP$^+$ cells per horizontal brain slice from the mice described in **a**. GFP$^+$ cells were identified using ilastik/CellProfiler, as described in the 'Image analysis' section of the Methods. **d**, Schematic of v3, v4 and v5 AAV variants. Arrows indicate the direction of U6 promoter transcription. The CBE3.9 coding sequence consists of rat APOBEC1 (teal), spCas9 D10A nickase (green) and UGI (orange). The small white boxes in v3 are non-essential backbone sequences removed in v4 and v5 AAV (see Supplementary Fig. 2 for a schematic of v5 AAV-ABEmax). **e**, Cytosine base-editing efficiencies at the *DNMT1* locus in NIH 3T3 cells seeded at 50,000 cells per well following a 14-day incubation with the indicated doses (darker data points: 10^{11} vg; lighter data points: 10^{10} vg) of v3, v4 and v5 AAV. Dots and bars in **b** and **c** represent individual replicates and mean + s.d. of $n=2$ (bGH and W3-bGH) or $n=3$ mice (WPRE-bGH). Coloured circles and error bars in **e** represent mean ± s.d. Dots in **e** represent values for independent biological replicates ($n=3$–4).

sgRNA and Cbh promoter. Notably, in side-by-side comparisons measuring base editing in three tissues, split intein-spliced v5 AAV-ABE on average provided 4.5-fold higher base-editing efficiencies than *trans*-RNA-spliced ABE (Fig. 3c). These results suggest that intein-mediated base-editor protein splicing is more efficient than base-editor mRNA *trans*-splicing. This efficiency difference may arise from the requirements of AAV genome concatemerization[38] followed by transcription and splicing of the ITR sequences, which have been reported to destabilize pre-mRNA[39], for successful *trans*-mRNA splicing.

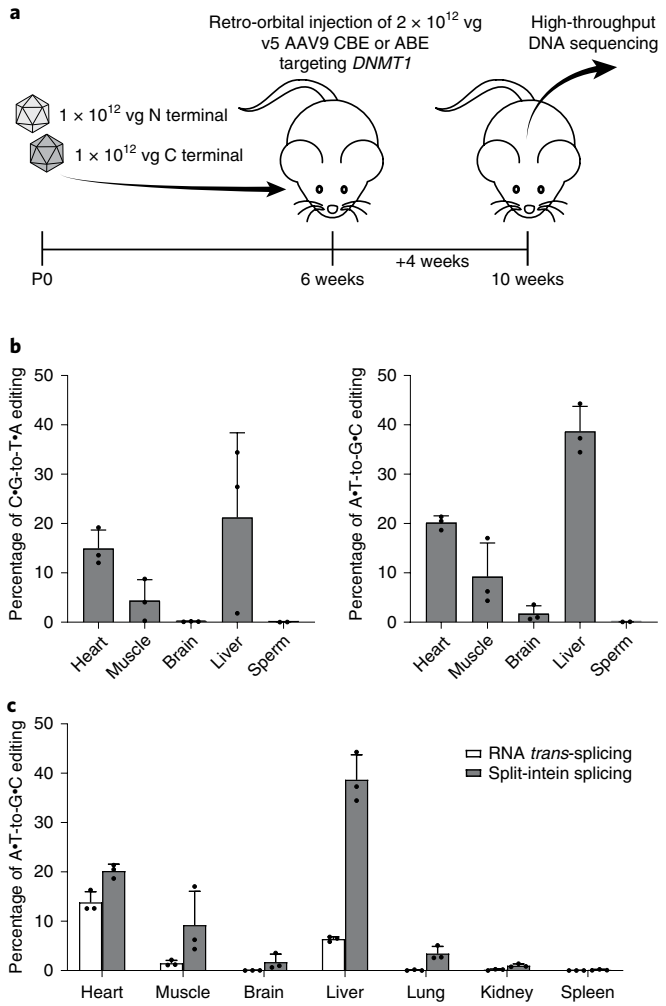

Fig. 3 | Systemic injection of v5 AAV9 editors results in cytosine and adenine base editing in heart, muscle and liver. a, Schematic of the retro-orbital injection experiments. Six-week-old C57BL/6 mice were treated by retro-orbital injection of 2×10^{12} vg total of v5 AAV9. After 4 weeks, organs were harvested and the genomic DNA of unsorted cells was sequenced. **b**, Cytosine (left) or adenine (right) base editing targeting *DNMT1* by v5 AAV-CBE3.9max or v5 AAV-ABEmax, respectively, in the indicated organs. **c**, Comparison of adenine base editing by v5 AAV-mediated split-intein ABEmax (grey bars) and *trans*-mRNA spliced ABE[8] (white bars). The *trans*-splicing constructs were modified to enable direct comparison by replacing the muscle-specific Spc5-12 promoter with the Cbh promoter for ubiquitous expression, and replacing the *DMD*-targeting sgRNA with the *DNMT1*-targeting sgRNA. Bars in **b** and **c** represent mean + s.d. of $n=3$ mice.

Notably, base-editing efficiencies in heart and skeletal muscle from split-intein AAV9 constructs (Fig. 3) are comparable to or higher than gene-rescue efficiencies reported to improve phenotypes in Duchenne muscular dystrophy animal models[40,41], and editing in the liver is above the correction thresholds required for phenotypic improvement in several inborn errors of metabolism[42–44]. These findings suggest that the split-AAV base-editor systems reported here may be suitable for developing treatments to correct animal models of human genetic diseases. We further note that these constructs have been optimized for general editing efficiency, and not for application-specific improvements including tissue- or cell type-specific promoters, which could further improve their specificity and activity in therapeutically relevant cells. Tissues that are not well transduced by intravenous AAV9 injections may be transduced by other existing AAV variants, such as AAV4 transduction of the lung[45], or by different delivery routes, such as AAV9 transduction of kidney cells by retrograde ureteral infusion[46].

Recently, Villiger and coworkers[24] developed an intein-split *S. aureus* CBE. To compare those constructs with the v5 constructs described in this study, we generated a v5 *S. aureus* CBE using intein-split SaBE3.9max, which has the same NLS and codon optimizations as the *S. pyogenes* Npu-BE3.9max construct, and cloned it into our v5 AAV architecture. We then packaged dual-AAV genomes in AAV8 with an sgRNA designed to generate the *PCSK9* W8X mutation[31], injected either 1×10^{11} or 1×10^{12} total vg per animal retro-orbitally into 3-week-old mice, and harvested liver tissue for high-throughput sequencing 4 weeks after injection. The Villiger constructs were modified only by replacement of the liver-specific P3 promoter with Cbh, and the *Pah*-targeting guide with *PCKS9* W8X. At the higher dose, the constructs performed comparably (v5 AAV SaCBE: 20 ± 0.9% W8X-encoding alleles; Villiger SaCBE: 18 ± 1.6% W8X-encoding alleles). However, at the lower dose, we observed no reduction in editing by the v5 AAV SaCBE constructs (25 ± 6.0% W8X alleles) but a substantial reduction in the editing efficiency of the Villiger constructs (8.2 ± 3.2% W8X alleles) (Supplementary Fig. 3c). We conclude that the higher 1×10^{12} vg dose reaches an editing ceiling due to processes extrinsic to the base editor, such as host DNA repair processes or cell state-specific factors. At the lower dose of the Villiger constructs, the base editor itself is limiting. These results show that the v5 AAV SaCBE constructs can outperform the corresponding constructs developed by Villiger and coworkers.

Base editing in CNS by split-intein CBE and ABE AAV. The above results establish an in vivo CBE and ABE delivery solution for somatic tissues transduced following systemic AAV injection. However, delivery to the CNS is especially challenging. Although AAV9 has been reported[47] to cross the blood–brain barrier and transduce CNS cells, we observed minimal editing in the brain following adult retro-orbital injection (Fig. 3). To enable in vivo base editing of cells in the CNS, we explored three complementary approaches. First, we performed neonatal cerebroventricular (postnatal day 0 (P0) intracerebroventricular (ICV)) injections. Similar to intrathecal injections currently used to deliver nusinersin to treat patients with spinal muscular atrophy[48], ICV injections are direct injections into cerebrospinal fluid. Second, we performed retro-orbital injections in 6-week-old mice using split-intein base-editor AAV based on PHP.eB—a laboratory-evolved AAV9 variant with improved ability to penetrate the blood–brain barrier in C57BL/6 mice[49–51]. Finally, we performed sub-retinal injections to directly transduce retinal tissue, given that AAV-mediated retinal transduction has already been shown to treat ocular disorders[11].

For all of the CNS delivery experiments, we combined dual split-intein CBE or ABE v5 AAV targeting *DNMT1* together with an AAV encoding a Cbh promoter-driven EGFP fused to a nuclear membrane-localized Klarsicht/ANC-1/Syne-1 homology (KASH) domain[22], hereafter referred to as GFP–KASH, to enable fluorescence-activated cell sorting isolation of cells with GFP-positive nuclei. Sorting for GFP$^+$ cells enriches cell types that are transducible by AAV and that can transcribe genes from the Cbh promoter. This enrichment is especially useful in the CNS, where the heterogeneity of interspersed cell types limits enrichment from physical dissection alone. For example, in the cerebellum, only Purkinje neurons, comprising <1% of total cerebellar tissue[52,53], are well transduced by known AAV variants at P0 (refs. [54,55]). However, these neurons are critically important as their degeneration causes a number of cerebellar ataxias[56,57]. Fluorescence-activated cell sorting isolation facilitates quantification of editing in this sparse population,

as shown by comparison of editing among sorted and unsorted cell populations (Fig. 4).

To determine optimal AAV variants for P0 ICV injections, we co-injected 4×10^{10} vg total of v5 AAV-CBE with 1×10^{10} vg of GFP–KASH (Fig. 4a). We tested four AAV variants that we hypothesized would efficiently transduce CNS cells following these neonatal direct brain injections: AAV8 and AAV9 (which have both been reported to transduce neurons following P0 injections[54]) and laboratory-evolved PHP.B and PHP.eB AAV variants[26,49] (which efficiently transduce CNS tissue in older mice). Measurements of GFP$^+$ nuclei by flow cytometry showed that in cortical tissue, transduction percentages varied from 43 ± 2.2% (AAV8) to 65 ± 4.4% (PHP.eB). In cerebellar tissue, none of the four serotypes efficiently transduced cells (AAV8: 0.8 ± 0.4%; AAV9: 2.7 ± 0.7%; PHP.B: 1.6 ± 0.2%; PHP.eB: 2.5 ± 0.5%) (Fig. 4b). The low transduction in the cerebellum is consistent with previous reports that Purkinje neurons represent nearly all cerebellar neurons transduced following P0 injections[54,55,58]. To confirm that transduced cerebellar cells were Purkinje neurons, we injected *L7-GFP* mice, which express cytoplasmic GFP in Purkinje neurons, with an mCherry-expressing AAV9 construct, and observed robust transduction only in GFP$^+$ cells (Supplementary Fig. 4a,b). Importantly, most Purkinje neurons were transduced, suggesting that the GFP$^+$ nuclei in Fig. 4b reflect a relatively large and unbiased sample of the overall Purkinje cell population. Taken together, these results suggest that all four variants transduce CNS cells with comparable efficiency.

Next, we sequenced cerebellar and cortical tissue. In cortex, we found that all four tested AAV variants mediated comparable and efficient C•G-to-T•A base editing among GFP$^+$ cells (65–70% base editing), as well as among unsorted cells (32–50% base editing) (Fig. 4c). In cerebellum, all four AAV variants again resulted in comparable and efficient base editing (Fig. 4c), resulting in 35–52% editing among GFP$^+$ cells. Since Purkinje neurons form the vast majority of transduced cerebellar cells[54,55,58] but represent only a small percentage of cerebellar tissue, base editing in unsorted cerebellar tissue was inefficient as expected, ranging from 0.52% (AAV8) to 2.5% (AAV9).

Having demonstrated cytosine base editing in the brain with AAV-CBE, we next tested adenine base editing with AAV-ABE. Since all AAV variants tested produced similar CBE3.9max base-editing efficiencies, we characterized P0 ICV injections of v5 AAV-ABE using AAV9. We observed that AAV9-delivered split-intein ABE edited cortex with high efficiency (87 ± 4.0% A•T-to-G•C editing among GFP$^+$ cells; 43 ± 9.1% editing among unsorted cells) and cerebellum (64 ± 5.6% among GFP$^+$ cells; 1.3 ± 0.5% among unsorted cells, consistent with the small percentage of Purkinje neurons in cerebellum) (Fig. 4d).

Although direct CNS injections resulted in robust base editing in the brain, we also sought to determine whether peripheral delivery of AAV via intravenous injection might efficiently edit the CNS, since intravenous injections offer substantial convenience, cost and safety advantages. We injected 4×10^{12} vg of PHP.eB encoding v5 AAV-CBE mixed with 2×10^{11} vg GFP–KASH retro-orbitally into 9-week-old mice (Fig. 4e). After 3–4 weeks, we harvested and sorted brain tissue. We observed highly efficient C•G-to-T•A base editing in cortex (74 ± 1.2% among GFP$^+$ cells; 59 ± 3.0% among unsorted cells) and cerebellum (70 ± 2.6% among GFP$^+$ cells; 35 ± 3.0% among unsorted cells; Fig. 4f). These data indicated that, in contrast with P0 ICV injection, intravenous injection of PHP.eB AAV in adult mice results in robust base editing in unsorted cerebellar tissue. Unlike the restrictive tropism observed at P0, in adult mice, retro-orbital injection of PHP.eB transduces several cell types in cerebellum. including granule cells and Olig2$^+$ oligodendrocytes[26]. This broadened tropism could be due to injection-route differences or expression differences over time in proteins that mediate AAV transduction. Collectively, these findings establish high-efficiency cytosine and adenine base editing in the CNS of a mammal.

In vivo base editing of retinal cells. Genome-editing approaches to treating inherited ocular disorders are of special interest given the accessibility of the eye, its immune-privileged status and the prevalence and impact of congenital blindness. We therefore tested the ability of sub-retinal injections of v5 AAV-ABE or v5 AAV-CBE to efficiently base edit photoreceptors and other retinal cells. We bred rhodopsin-Cre mice, which express Cre only in retinal rod photoreceptor cells, with Ai9 mice[59] to generate mice that express tdTomato only in rod photoreceptor cells. We performed sub-retinal injections of v5 AAV-CBE or v5 AAV-ABE targeting *DNMT1* in 2-week-old mice (Fig. 5a). We tested two AAV variants that have been shown to transduce retinal tissue: PHP.B[26] (which performs similarly to AAV9/PHP.eB above in P0 injections) and Anc80 (which contains a computationally reconstructed ancestral AAV capsid sequence and has previously been shown to transduce rods more efficiently than AAV8 (ref. [60])). PHP.B-Cbh-GFP–KASH or Anc80-Cbh-GFP–KASH was co-injected as a marker for transduced cells.

Three weeks post-injection, we sorted retinal cells into GFP$^+$/tdTomato$^+$ (transduced rods), GFP$^+$/tdTomato$^-$ (marker transduced non-rods), GFP$^-$/tdTomato$^+$ (unmarked rods) or double-negative (unmarked non-rods) cells. PHP.B-GFP–KASH-transduced 65 ± 2.8% of rods and 9.6 ± 1.4% of non-rods, while a sixfold lower dose of Anc80-GFP–KASH-transduced cells much less efficiently (Fig. 5b). When delivered at the same dose (5×10^9 vg), both PHP.B and Anc80 showed comparable transduction efficiency in the retina, and the majority of cells transduced by both variants were photoreceptors (Fig. 5c). Both PHP.B and Anc80 AAV efficiently delivered split-intein base editors into retinal cells, with PHP.B-mediated v5 AAV-CBE resulting in 48 ± 5.9% C•G-to-T•A editing among GFP$^+$/tdTomato$^+$ rod photoreceptors (19 ± 8.7% among all tdTomato$^+$ rods), and with Anc80-mediated v5 AAV-ABE resulting in 37 ± 22% A•T-to-G•C editing among GFP$^+$/tdTomato$^+$ rod photoreceptors (26 ± 16% editing among all rod photoreceptor cells) (Fig. 5d–f). These editing efficiencies—even among unsorted PHP.B-transduced rod photoreceptors—are similar to the frequencies of wild-type alleles required to improve retinal function in mosaic *Pde6b* mutant mice[61]. The editing efficiencies we observed are also comparable to those reported in preclinical data for EDIT-101—a single-vector AAV treatment for Leber congenital amaurosis that delivers Cas9 nuclease[62]—suggesting that dual-vector AAV co-transduction in retinal tissue can achieve therapeutically relevant editing efficiencies.

Interestingly, although ABE delivery generated very few indels in retinal cells, consistent with previous results from cultured cells[4], and both ABE and CBE delivery in non-retinal tissues in the experiments described above generally resulted in base edit-to-indel ratios >10:1 (Supplementary Table 1), CBE delivery to retinal cells generated substantial indels, with base edit-to-indel ratios between 2:1 and 1:1 and indel percentages up to 34%. Despite the substantial frequency of indels, there was little overlap between indel-containing and base-edited alleles. Excluding indel-containing reads did not reduce the number of reads with C•G-to-T•A editing (Supplementary Fig. 5a,b), indicating that base-edited alleles in general do not contain indels. These observations suggest that CBE-mediated indels in retinal cells occur through uracil excision pathways that are mutually exclusive with pathways that lead to cytosine base-editing outcomes, or that base-edited or indel-containing products are poor substrates for subsequent indel-generating or base-editing processes, respectively.

In vivo correction of a causal Niemann–Pick mutation in mouse CNS. Integrating the above developments, we applied AAV-mediated in vivo base-editor delivery to correct a mutation associated with human disease in the CNS of an animal. *NPC1* mediates intracellular lipid transport, and loss-of-function mutations cause NPC disease—a neurodegenerative ataxia. *NPC1* c.3182T > C

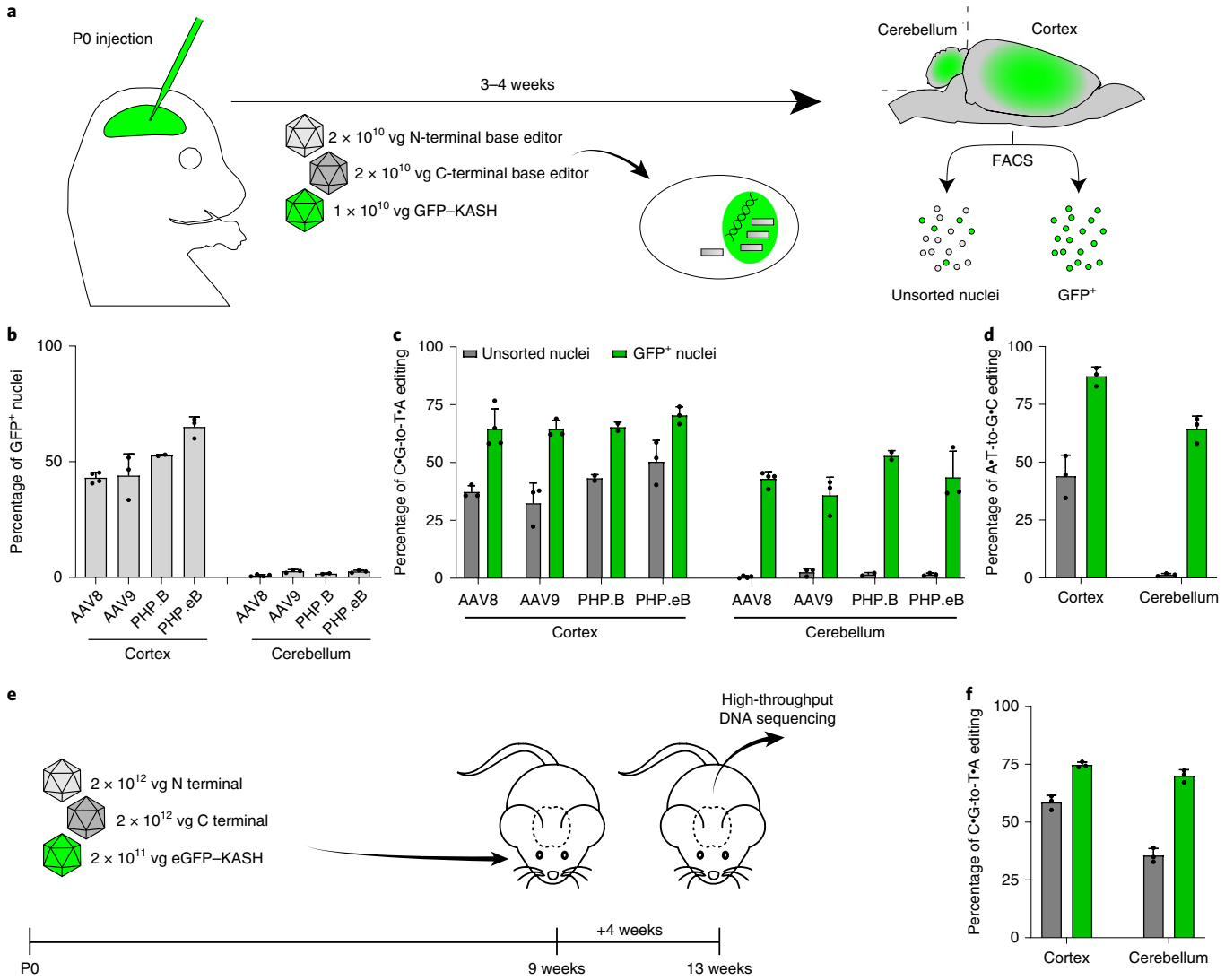

Fig. 4 | AAV-mediated cytosine and adenine base editing in the CNS by two delivery routes. a, Schematic of the P0 intraventricular injections. P0 C57BL/6 mice were co-injected with 4×10^{10} vg total of v5 CBE3.9max or ABEmax AAV targeting *DNMT1* and 1×10^{10} vg Cbh-GFP–KASH. Sorting for GFP$^+$ cells enriches for triply transduced cells. Tissue was harvested 3–4 weeks after injection, and cortex and cerebellum were separated. Cortical tissue comprises neocortex and hippocampus. For each tissue, nuclei were dissociated and analysed as unsorted (all nuclei) or GFP$^+$ populations for DNA sequencing. FACS, fluorescence-activated cell sorting. **b**, Percentage of GFP$^+$ nuclei measured by flow cytometry following P0 injection. **c**, Cytosine base-editing efficiency following P0 v5 CBE3.9max AAV-CBE injection in cortex and cerebellum at *DNMT1* for unsorted (grey) and GFP$^+$ (green) nuclei using the indicated serotypes. In **b** and **c**, $n=4$ for AAV8, $n=3$ for AAV9, $n=2$ for PHP.B and $n=3$ for PHP.eB. **d**, Adenosine base-editing efficiency following P0 v5 CBE3.9max AAV9-ABE injection in cortex and cerebellum at *DNMT1* for unsorted (grey) and GFP$^+$ (green) nuclei ($n=3$). **e**, Schematic of the retro-orbital injections. Brains from 9-week-old C57BL/6 mice were harvested 4 weeks after injection with 4×10^{12} vg total v5 PHP.eB CBE3.9max or ABEmax AAV targeting *DNMT1* and 2×10^{11} vg PHP.eB GFP–KASH AAV, then processed and analysed as described in **a**. **f**, Cytosine base editing in unsorted (grey) and GFP$^+$ (green) cortical and cerebellar cells following the procedure described in **e**, then processed and analysed as described in **a** ($n=3$). In all cases, bars represent mean + s.d. Black dots represent individual mice.

(encoding Ile1061Thr) is the most prevalent mutation in humans that causes NPC disease[63,64]. Previous work suggests that Niemann–Pick disease is primarily a CNS disorder; genetic deletion of *Npc1* in the CNS alone causes Niemann–Pick disease in mice[65], while expression of wild-type *Npc1* in the CNS alone prevents the disease[66,67]. Furthermore, deletion of *Npc1* in Purkinje neurons alone causes motor impairment[68]. Chimeric mouse studies suggest that the death of Purkinje neurons is cell autonomous and therefore amenable to mosaic rescue[69]. *Npc1*^{I1061T} homozygous mice develop ataxia and have a reduced lifespan of approximately 17 weeks[64], while chimeric mice with ≥15–32% wild-type alleles show modest but detectable increases in lifespan and reduced ataxia[69].

To test whether base editing of *Npc1* c.3182T>C in the CNS might extend lifespan, we injected P0 *Npc1*^{I1061T} (c.3182T>C) homozygous mice with 4×10^{10} or 1×10^{11} vg total AAV9 encoding v5 AAV-CBE (2×10^{10} or 5×10^{10} vg of each AAV half) targeting the *Npc1* I1061T mutation, and 1×10^{10} vg of GFP–KASH, which we refer to as low dose and high dose, respectively. Cytosine base editing at this site should directly revert the 3182T>C mutation (Fig. 6a). Although we found no difference in lifespan between low-dose and untreated mice (Fig. 6b), high-dose mice survived 9.2% longer than untreated mice (Fig. 6b; median survival increases from 102.5 to 112 d; $\chi^2=5.358$; d.f. = 1; $P=0.02$, Mantel–Cox test). Given the modest lifespan increase, we treated a second cohort of five *Npc1*^{I1061T}

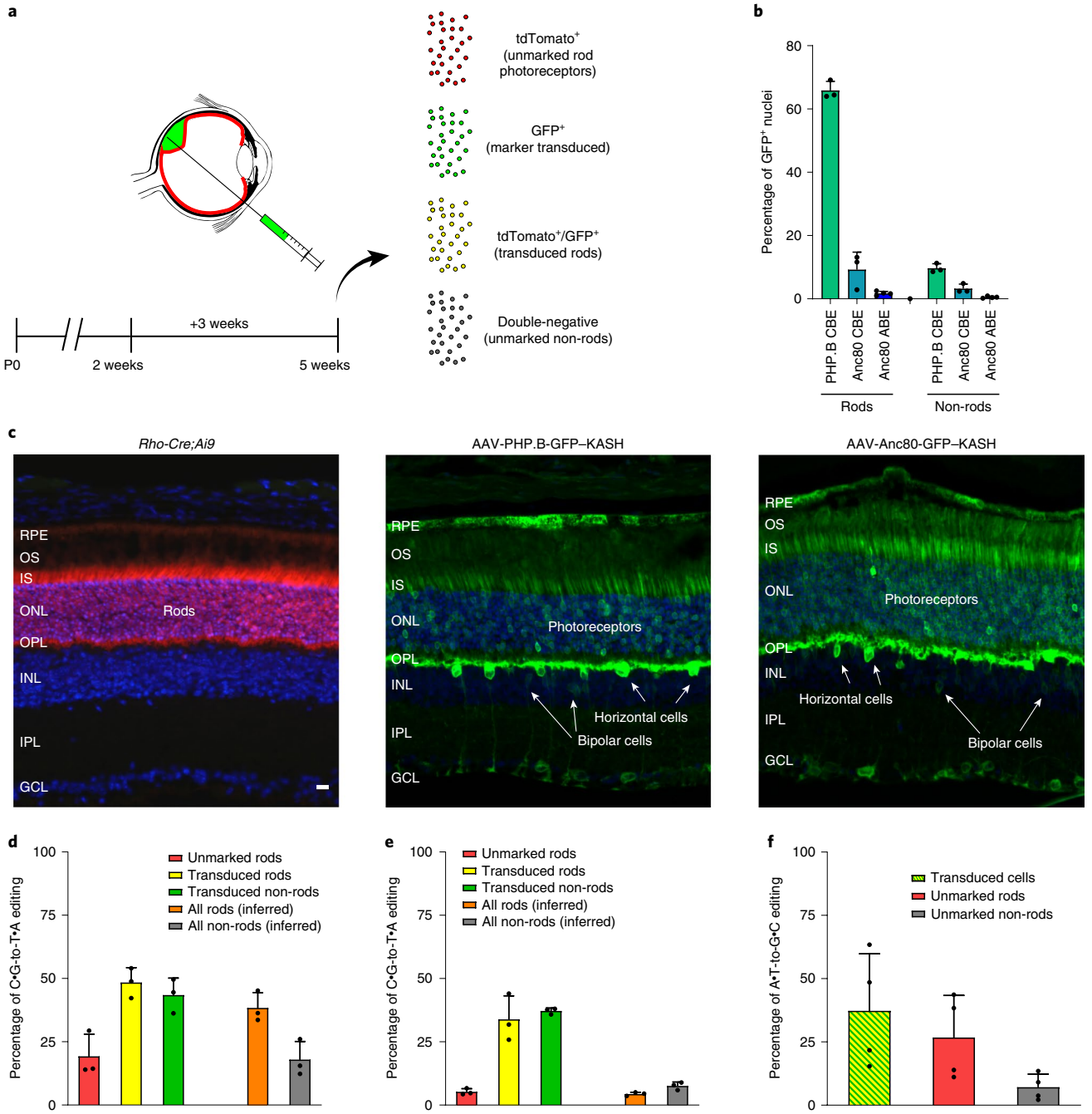

Fig. 5 | AAV-mediated cytosine and adenine base editing in the retina following sub-retinal injections of 2-week-old *Rho-Cre;Ai9* mice. a, Schematic of sub-retinal injections. Two-week-old *Rho-Cre;Ai9* mice were treated by sub-retinal injection of 1×10^{9}–1×10^{10} vg total of GFP–KASH and v5 CBE3.9max or v5 ABEmax AAV targeting *DNMT1*. Three weeks after injection, injected retinas were sorted into GFP$^-$/tdTomato$^+$ (rod photoreceptors not transduced with GFP; red), tdTomato$^+$/GFP$^+$ (transduced rods; yellow), GFP$^+$/tdTomato$^-$ (marker transduced non-rods; green) and double-negative populations (unmarked non-rods; grey). **b**, Percentage of GFP-transduced rod photoreceptors or non-rod retinal cells following sub-retinal injection of GFP–KASH AAV mixed with PHP.B-CBE, Anc80-CBE or Anc80-ABE AAV. The doses of GFP–KASH were 2×10^{9} vg for PHP.B-CBE mix, 3.3×10^{8} vg for Anc80-CBE mix and 4.5×10^{8} vg for Anc80-ABE mix. **c**, Left: expression of tdTomato in the rod photoreceptor cells of *Rho-Cre;Ai9* mice. Middle: retinal transduction of PHP.B GFP–KASH at 5×10^{9} vg. Right: retinal transduction of Anc80 GFP–KASH at 5×10^{9} vg. Scale bar, 20 µm. The images are representative of $n=2$ independent experiments. GCL, ganglion cell layer; INL, inner nuclear layer; IPL, inner plexiform layer; IS, inner photoreceptor segments; ONL, outer nuclear layer; OPL, outer plexiform layer; OS, photoreceptor outer segment; RPE, retinal pigment epithelium. **d**, Cytosine base editing by v5 CBE3.9max PHP.B AAV targeting *DNMT1* in injected retinas. Retinas were injected with 6.5×10^{8} vg of each split-editor half. The editing percentage in all rods was inferred as ((editing percentage in GFP-transduced rods) × (number of transduced rods) + (editing percentage in unmarked rods) × (number of unmarked rods))/total rods. This calculation was repeated for non-rods. **e**, Cytosine base editing by v5 CBE3.9max Anc80 AAV targeting *DNMT1* in photoreceptors and other retinal cells. Retinas were injected with 4×10^{9} vg of each split-editor half. Editing efficiencies in all rods and all non-rods were inferred as described in **d**. **f**, Adenine base editing by v5 ABEmax Anc80 AAV targeting *DNMT1* in photoreceptors. Retinas were injected with 4.5×10^{8} vg of each split-editor half. All GFP$^+$ cells were pooled in this experiment, resulting in a single GFP$^+$ population containing tdTomato$^+$ and tdTomato$^-$ cells (yellow/green bar). Black dots represent individual eyes. For **b** and **d**–**f**, bars represent mean + s.d. of independent injections ($n=3$ for PHP.B-CBE, $n=3$ for Anc80-CBE and $n=4$ for Anc80-ABE).

mice using retro-orbital injections of 3×10^{12} vg v5 PHP.eB-CBE and 1×10^{12} vg AAV9-CBE at P30–P40. Consistent with the results of the first cohort, this second treated cohort survived 10% longer than untreated mice (Supplementary Fig. 6a; median survival increased from 109 to 120 d; $\chi^2=5.911$; d.f. = 1; $P=0.015$, Mantel–Cox test). Taken together, these findings suggest that in vivo AAV-delivered base editing to correct *Npc1* c.3182T > C modestly extends the lifespan of treated mice.

To determine whether v5 AAV9-CBE injection increases the number of surviving Purkinje neurons, we compared a cohort of age-matched injected and untreated mice at P98–P105 (close to the lifespan of the untreated mice). In agreement with the observed lifespan extension, injection of AAV9 AAV-CBE increased the number of surviving Purkinje neurons from 24% of the wild-type value to 38% of the wild-type value (uninjected: 5.1 ± 1.2 Purkinje neurons per mm of Purkinje cell layer; injected: 8.0 ± 0.8 Purkinje neurons per mm; wild type: 21.1 ± 5.5 Purkinje neurons per mm; uninjected versus injected: $P=0.03$) (Fig. 6c). Quantitatively similar increases in Purkinje cell survival mediated by small molecules in *Npc1*$^{-/-}$ mice have previously been associated with lifespan increases similar to those we observed[70]. These results show that AAV-mediated CNS base editing of *Npc1* increases the survival of Purkinje neurons to an extent consistent with the lifespan increase of the treated mice. To further probe the possibility that *Npc1* base editing improves cellular markers of NPC1 disease, and to determine whether the CBE-mediated mosaic rescue might provide systemic benefits, we examined CD68$^+$ reactive microglia—a measure of CNS inflammation[67,71]. We quantified the density of CD68$^+$ cells and total CD68$^+$ tissue area in mice injected with AAV9 AAV-CBE, finding modest decreases in CD68$^+$ tissue area in agreement with the modest increase in Purkinje cell survival (Fig. 6d; decrease from 19.9 ± 0.05 to 16.7 ± 0.08%; $P=0.005$; see single-channel images included in Supplementary Fig. 7a). Although CD68$^+$ cell density decreased from 913 ± 26 to 850 ± 30 cells per mm^2, this difference was not statistically significant (Supplementary Fig. 7b; $P=0.15$).

Finally, we euthanized mice from the survival cohort at the onset of morbidity to harvest brain tissue for high-throughput DNA sequencing, and sorted GFP$^+$ cortical and cerebellar nuclei as described above (Fig. 4). In mice given a low dose of v5 AAV-CBE, the *Npc1* c.3182T > C mutation was corrected with 31 ± 16% efficiency in unsorted cortical nuclei, and in 46 ± 22% of GFP$^+$ nuclei. In cerebellum, we observed editing of 0.4 ± 0.5% in unsorted tissue and 11 ± 8.4% in GFP$^+$ nuclei, which correspond to the critical Purkinje cell population that must be edited to treat NPC disease. In high-dose mice, we observed cortical editing of 48 ± 8.2 and 81 ± 3.7% in unsorted and sorted nuclei, respectively, and target cerebellar editing of 0.3 ± 0.2 and 42 ± 14% of unsorted and sorted nuclei, respectively (Fig. 6e). In all cases, C-to-T editing without bystander edits or indels was predominant among edited alleles; over 94% of edited alleles precisely correct the c.3182T > C mutation and encode the wild-type allele (Fig. 6e; indels reported in Supplementary Table 1). We also determined whether off-target editing might occur in the sorted cerebellar and cortical nuclei. We identified candidate loci using two methods: we used CRISPOR (a bioinformatic method to predict off-target sites with Cas9 activity) and we empirically determined off-target Cas9 loci using CIRCLE-Seq on genomic DNA harvested from the liver of an untreated *Npc1*^{I1061T} mouse. We then performed amplicon sequencing to confirm editing at eight total candidate loci identified by either method. We observed only a single confirmed off-target site: an intronic sequence in *Epas1* >3 kb away from the nearest exonic sequences, which was edited at a low efficiency of 0.3 ± 0.05% (Supplementary Fig. 8).

Previous work with mosaic mice has shown that approximately 15–32% wild-type *Npc1* alleles are required for modest but measurable phenotypic improvement and lifespan extension[69]. Since the above data suggest ~11% Purkinje cell editing in low-dose mice with no lifespan extension and ~42% Purkinje cell editing in high-dose mice with modest but significant lifespan extension, our results are wholly consistent with the modest lifespan gains observed in mosaic mice with similar proportions of wild-type alleles[69].

We note that unedited cells may have degenerated; thus, editing levels in sequenced tissue represent upper limits of the initial percentage of edited cells. To minimize the effect of degeneration on the frequency of edited cells, we measured base editing in heterozygous *Npc1*$^{I1061T/+}$ mice, which do not show NPC disease phenotypes, following high-dose P0 injections. At P29, we found 31 ± 5.8% of GFP$^+$ cerebellar nuclei were edited, which increased to 54 ± 10% at P110. In sorted cortical nuclei, the percentage of edited cells increased from 59 ± 5.4 to 82 ± 7.2% (Supplementary Fig. 9a), suggesting that C•G-to-T•A editing continues for more than 4 weeks after P0 injection. To test whether CBE is chronically expressed, we injected *Npc1*$^{+/+}$ mice with v5 AAV-CBE at P0 and harvested brains at P110 for staining against Cas9 and GFP. We observed expression of both Cas9 and GFP at P110 in cerebellar and cortical tissue

Fig. 6 | Base editing of *Npc1*^{I1061T} in the mouse CNS. a, Schematic of the *Npc1* locus, highlighting the mutation in exon 21, the protospacer and protospacer-adjacent motif (PAM) sequence targeted, and the desired CBE-mediated reversion of I1061T. **b**, Kaplan–Meier plots of untreated homozygous *Npc1*^{I1061T} mice (red; $n=14$), *Npc1*^{I1061T} heterozygous mice (black; $n=14$) and mice injected with either 4×10^{10} vg total of v5 CBE3.9max AAV9 targeting *NPC1*^{I1061T} (left; blue; $n=7$) or 1×10^{11} vg total v5 CBE3.9max AAV9 targeting *Npc1*^{I1061T} (right; blue; $n=5$). Following 1×10^{11} vg injection, the median survival increased from 102.5 to 112 d ($P=0.02$, Mantel–Cox test). **c**, Immunofluorescence measurements of Purkinje cell survival. Images are representative Calbindin-stained midline sagittal cerebellar slices from P98–P105 mice. Surviving calbindin$^+$ cells appear in green, while DAPI is pseudocoloured magenta. In the quantification of the imaging data (right), each point represents the average number of Purkinje cells per slice for each mouse (wild type: $n=3$ mice; $n=9$ images; *Npc1*^{I1061T} untreated: $n=5$ mice; $n=20$ images; *Npc1*^{I1061T} AAV-CBE: $n=2$ mice; $n=16$ images). For the comparison of untreated versus treated, a two-sided *t*-test was used (*$P=0.0327$). **d**, Immunofluorescence measurements of CD68$^+$ tissue area. Images are representative CD68-stained midline saggital cerebellar slices from P98–P105 mice. EGFP–KASH-labelled cells appear in cyan, CD68$^+$ cells appear in yellow and the DRAQ5 signal is pseudocoloured magenta. The untreated mice were not injected and did not express GFP. In the quantification of CD68$^+$ tissue area (right), each point represents the average per mouse (wild type: $n=3$ mice, $n=15$ images; *Npc1*^{I1061T} untreated: $n=2$ mice, $n=6$ images; *Npc1*^{I1061T} AAV-CBE: $n=2$ mice, $n=10$ images). For the comparison of untreated versus treated, a two-sided *t*-test was used (***$P=0.0005$). **e**, Cortical and cerebellar base editing in P0 mice injected with v5 CBE3.9max AAV9 targeting *Npc1*^{I1061T}. Left: lighter bars report editing in unsorted (grey) or GFP$^+$ cells (green) following injection of $n=3$ mice with 4×10^{10} vg v5 CBE3.9max (2×10^{10} vg of each split base-editor half), while darker bars correspond to editing following injection of $n=5$ mice with 1×10^{11} vg v5 CBE3.9max (5×10^{10} vg of each split base-editor half). Middle: base editing to the precisely corrected wild-type allele shown in **a** from the 1×10^{11} vg injections, where lighter bars indicate the frequency of alleles that were corrected to the wild-type sequence and re-plotted darker bars indicate total C•G-to-T•A editing of the T1061 codon coloured red in **a**. Right: precisely corrected (wild-type) alleles as a percentage of all edited alleles in mice injected with 1×10^{11} vg v5 CBE3.9max AAV9 targeting *NPC1*^{I1061T}. In **b**, tick marks indicate animal deaths. In **c**–**e**, bars represent mean + s.d. Dots represent individual mice. In **c** and **d**, scale bars represent 200 μm. Two-sided *t*-tests without multiple comparison corrections were used to test for the statistical significance of immunofluorescence.

(Supplementary Fig. 9b,c), suggesting that, consistent with previous studies, AAV mediates long-term neuronal transgene expression. Although the above data are consistent with a prolonged editing activity window, and although *Npc1*$^{+/-}$ heterozygotes do not have any cellular markers of disease[67], we cannot rule out the possibility that the apparent continued editing in heterozygotes may simply be the result of a survival advantage in edited cells.

These results establish that dual-AAV split-intein base-editor delivery in mice with NPC directly corrects a substantial fraction of pathogenic alleles in the CNS. Together, these results show the use of base editing to treat an animal model of a human CNS disease.

Discussion

This study describes an optimized dual-AAV system that delivers split-intein CBEs and ABEs, resulting in therapeutically relevant in vivo genome-editing efficiencies following injection of ~10^{13}–10^{14} vg kg^{-1}—a dosage comparable to those currently used in human gene therapy trials[32]. The optimizations described above greatly

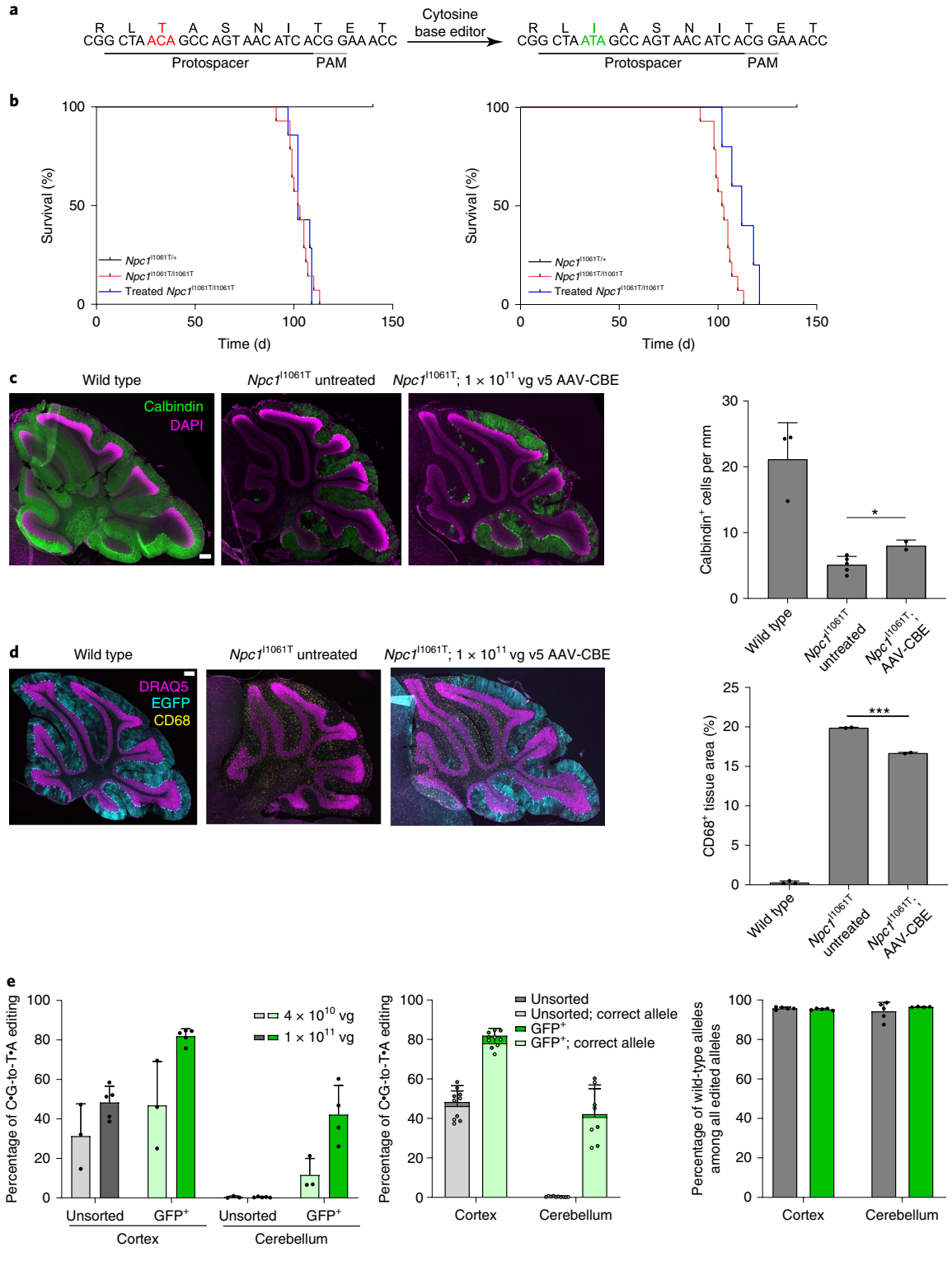

improve the efficiency of AAV-encoded base editors and may also be useful to other AAV-based systems for the delivery of genome-editing agents[8,24]. Many somatic cell types of therapeutic and scientific interest can be efficiently transduced with known AAV variants, including haematopoietic cells[72], liver[73], sensory organs[11] and CNS[32], suggesting that this work may facilitate a broad range of studies in animal models of many human genetic diseases. Finally, we tested different injection routes to deliver AAV-packaged split base editors in postnatal mice, and demonstrate efficient base editing in brain and retina, enabling causal gene correction of NPC disease. Previous work has shown that gene augmentation by AAV9-delivered *Npc1* significantly increases lifespan in *Npc1*$^{-/-}$ mice[71,74,75]. *Npc1* gene augmentation appears to improve lifespan more than the split-editor constructs described here, although the delivery efficiency appears similar, potentially due to gene augmentation producing functional *Npc1* in all transduced cells without requiring additional mechanistic steps. Further improvements to the base editors and AAV architecture may improve phenotypic rescue in this setting.

The mouse studies described here use AAV injections of no more than 4×10^{12} vg per 20-g animal, which corresponds to a maximum dose of 2×10^{14} vg kg^{-1}, consistent with the maximum dosages delivered intravenously in non-human primate studies[76] and clinical trials[32] for CNS delivery. Notably, in the eye, sub-retinal injections of our optimized base-editor AAVs achieve genome-editing efficiencies comparable to those of preclinical delivery systems optimized for retinal editing[62]. Intravenous v5 AAV injections also achieve therapeutically relevant editing levels in liver, muscle and cardiac tissue. The viral base-editing systems developed in this study are therefore suitable for testing base-editing strategies in animal models of human disease—a key step in advancing base editing towards human therapeutic application. AAV optimization (Fig. 2) reduced the viral dose required for efficient base editing to amounts known to be tolerated by humans, enabling more practical and therapeutically relevant editing in animal models of human genetic diseases compared with the much higher doses previously used in *trans*-splicing mRNA viral vectors[8].

While we initially anticipated that the requirement of simultaneous transduction by two viruses would sharply lower editing efficiencies, the surprisingly high overall in vivo editing efficiencies we observed even among unsorted cells (for example, up to 59% of cortex), together with similar levels of transduction of single AAVs expressing GFP as levels of edited cells that required dual-AAV transduction (Fig. 4b), strongly suggest that transducible cells are particularly amenable to transduction by multiple AAVs. Editing efficiency may be further increased by tissue-specific optimization such as selection of a delivery route that biases AAV concentrations towards relevant tissues, such as hepatic artery injections to transduce liver[77], and tissue-specific promoter and terminator variation to enhance expression in specific cell types.

The split-intein base-editor delivery system developed here brings the strengths of base editing, including high editing efficiency, minimization of unwanted byproducts arising from double-stranded DNA breaks, and compatibility with post-mitotic somatic cells[2,9] to in vivo settings in the diverse tissue types that are well transduced by natural or engineered AAVs. The split-intein dual-AAV approach described here may also facilitate the in vivo delivery of genes that are too large for a direct gene augmentation approach.

Methods

Molecular biology. All expression vectors used for HEK293T transfection were generated by Gibson cloning. All sgRNA constructs were generated by ligation of annealed oligos into pFYF1320 modified to contain a BsmBI dummy spacer that leaves 5′-CACC and 5′-CAAA overhangs compatible with general sgRNA cloning techniques (for example, https://www.addgene.org/crispr/zhang/). AAV vectors were generated by Gibson cloning of PCR-amplified inserts into restriction enzyme-digested backbones.

Cell culture. HEK239T/17 (American Type Culture Collection (ATCC); CRL-11268) and 3T3 cells (ATCC; CRL-1658) were maintained in DMEM (Thermo Fisher Scientific; 10569044) supplemented with 10% (*v*/*v*) foetal bovine serum (Thermo Fisher Scientific), at 37 °C with 5% CO_2. Cells were verified to be free of mycoplasma by the ATCC upon purchase, and periodically during culture. For cell culture experiments, transfections of independently maintained cell lines, or different passages of the same cell line, were considered biologically independent measurements.

HEK293T and 3T3 transfection and genomic DNA preparation. HEK293T cells were seeded into 48-well poly-D-lysine-coated plates (Corning; 354509) at 30,000 cells per well. One day after plating, cells were transfected by Lipofectamine 2000 (Thermo Fisher Scientific), according to the manufacturer's instructions, with 1 µg DNA in a 1:1 molar ratio of base editor and sgRNA plasmids, plus 10 ng of fluorescent protein expression plasmid as a transfection control. Cells were cultured for 3 d before genomic DNA was extracted by replacement of the culture media with 100 µl lysis buffer (10 mM Tris-HCl (pH 7.5), 0.05% sodium dodecyl sulfate and 25 µg ml^{-1} proteinase K (NEB)) and 37 °C incubation for 1 h. Proteinase K was inactivated by 30-min incubation at 80 °C. 3T3 cells were transfected using the same procedure at 50,000 cells per well. For the AAV experiments, 10^{10}–10^{11} vg were added to wells containing 50,000 3T3 cells, resulting in multiplicity of infection values of 2×10^{5}–2×10^{6} vg per cell.

Western blotting. HEK293T cells were seeded into 12-well plates at 125,000 cells per well. Cells were transfected as described above with all amounts scaled up 3×. For conditions with transfection of only one split half, EGFP-expressing plasmid was used to normalize the amount of DNA used. Three days after transfection, cells were gently lifted and triturated by pipetting phosphate-buffered saline (PBS) across the well surface. Then, 10% of the volume was removed for high-throughput sequencing and the remaining cells were washed with ice-cold PBS and incubated on ice for 15 min in lysis buffer (300 mM NaCl, 50 mM Tris (pH 8), 1% IGEPAL, 0.5% deoxycholic acid and 10 mM MgCl) plus 25 U ml^{-1} salt active nuclease (ArcticZymes; 70910-202), to reduce lysate viscosity, and cOmplete EDTA-free protease inhibitor cocktail (Roche). After 10 min, sodium dodecyl sulfate and EDTA were added to 0.5% and 1 mM, respectively, and lysates were rocked for an additional 15 min at 4 °C before clarification by centrifugation at 14,000*g* for 15 min at 4 °C. Lysates were normalized using BCA (Pierce BCA Protein Assay Kit), and 2.5 mg of reduced protein was loaded onto each gel lane. Transfer was performed with an iBlot 2 Dry Blotting System (Thermo Fisher Scientific) using the following programme: 20 V for 1 min, then 23 V for 4 min, then 25 V for 2 min, for a total transfer time of 7 min. Blocking was performed at room temperature for 30 min with block buffer: 1% bovine serum albumin (BSA) in TBST (150 mM NaCl, 0.5% Tween-20 and 50 mM Tris-Cl (pH 7.5)). Membranes were then incubated in primary antibody diluted in block buffer at 4 °C overnight. After a wash step, secondary antibodies diluted in TBST were added. Membranes were washed again and imaged using a LI-COR Odyssey. Wash steps were 3× 5-min washes in TBST. The primary antibodies used were rabbit anti-GAPDH (1:1,000; Cell Signaling Technologies; D16H11); rabbit anti-HA (1:1,000; Cell Signaling Technologies; C29F4), mouse anti-FLAG (1 µg ml^{-1}; clone M2; Sigma–Aldrich; F1804). LI-COR IRDye 680RD goat anti-rabbit (926-68071) and goat anti-mouse (926-68070) secondary antibodies were used at 1:10,000–1:20,000 dilutions.

High-throughput sequencing and data analysis. Genomic DNA was amplified by quantitative PCR (qPCR) using Phusion Hot Start II DNA polymerase with use of SYBR gold for quantification. Then, 3% DMSO was added to all genomic DNA PCR reactions. To minimize PCR bias, reactions were stopped during the exponential amplification phase. Afterwards, 1 µl of the unpurified genomic DNA PCR product was used as a template for subsequent barcoding PCR (eight cycles; annealing temperature: 61 °C). Pooled barcoding PCR products were gel extracted (MinElute columns; Qiagen) and quantified by qPCR (KAPA; KK4824) or Qubit dsDNA HS Assay Kit (Thermo Fisher Scientific). Sequencing of pooled amplicons was performed using an Illumina MiSeq according to the manufacturer's instructions. All oligonucleotide sequences used for genomic DNA amplification are provided in Supplementary Table 1.

Initial de-multiplexing and FASTQ generation were performed by bcl2fastq2 running on BaseSpace (Illumina) with the following flags: --ignore-missing-bcls --ignore-missing-filter --ignore-missing-positions --ignore-missing-controls --auto-set-to-zero-barcode-mismatches --find-adapters-with-sliding-window --adapter-stringency 0.9 --mask-short-adapter-reads 35 --minimum-trimmed-read-length 35. Alignment of fastq files and quantification of editing frequency was performed by CRISPResso2 in batch mode with the following flags: --min_bp_quality_or_N 20 --base_editor_output -p 2 -w 20 -wc -10. For the PCKS9 experiments, the total number of reads encoding Trp 8 to STOP (TAA, TGA and TAG) was summed and divided by the number of aligned reads.

AAV production. AAV production was performed as previously described[26] with some alterations. HEK293T/17 cells were maintained in DMEM/10% foetal bovine serum without antibiotic in 150-mm dishes (Thermo Fisher Scientific; 157150) and passaged every 2–3 d. Cells for production were split 1:3 1 d before

polyethylenimine transfection. Then, 5.7 µg AAV genome, 11.4 µg pHelper (Clontech) and 22.8 µg rep-cap plasmid were transfected per plate. One day after transfection, media was exchanged for DMEM/5% foetal bovine serum. Three days after transfection, cells were scraped with a rubber cell scraper (Corning), pelleted by centrifugation for 10 min at 2,000*g*, resuspended in 500 µl hypertonic lysis buffer per plate (40 mM Tris base, 500 mM NaCl, 2 mM $MgCl_2$ and 100 U ml^{-1} salt active nuclease (ArcticZymes; 70910-202)) and incubated at 37 °C for 1 h to lyse the cells. The media was decanted, combined with a 5× solution of 40% poly(ethylene glycol) (PEG) in 2.5 M NaCl (final concentration: 8% PEG/500 mM NaCl), incubated on ice for 2 h to facilitate PEG precipitation, and centrifuged at 3,200*g* for 40 min. The supernatant was discarded and the pellet was resuspended in 500 µl lysis buffer per plate and added to the cell lysate. Incubation at 37 °C was continued for 30 min. Crude lysates were either incubated at 4 °C overnight or directly used for ultracentrifugation.

Cell lysates were gently clarified by centrifugation at 2,000*g* for 10 min and added to Beckman Quick-Seal tubes via 16-gauge 5" disposable needles (Air-Tite N165). A discontinuous iodixanol gradient was formed by sequentially floating layers: 9 ml 15% iodixanol in 500 mM NaCl and 1× PBS-MK (1× PBS plus 1 mM $MgCl_2$ and 2.5 mM KCl), 6 ml 25% iodixanol in 1× PBS-MK, and 5 ml each of 40 and 60% iodixanol in 1× PBS-MK. Phenol red at a final concentration of 1 µg ml^{-1} was added to the 15, 25 and 60% layers to facilitate identification. Ultracentrifugation was performed using a Ti 70 rotor in a Sorvall WX+ series ultracentrifuge (Thermo Fisher Scientific) at 58,600 r.p.m. for 2 h 15 min at 18 °C. Following ultracentrifugation, roughly 4 ml of solution was withdrawn from the 40–60% iodixanol interface via an 18-gauge needle, dialysed with PBS containing 0.001% F-68, and ultrafiltered via 100-kD MWCO columns (EMD Millipore). The concentrated viral solution was sterile filtered using a 0.22-µm filter, quantified via qPCR (AAVpro Titration Kit version 2; Clontech), and stored at 4 °C until use.

Animals. All experiments in live animals were approved by the Broad Institute and Massachusetts Eye and Ear institutional animal care and use committees. Wild-type C57BL/6 mice were from Charles River Laboratories (027). The Jackson Laboratory supplied all transgenic mice: *Npc1*$^{tm(I1061T)Dso}$ (027704), Ai9 (007909), Rhodopsin-iCre (015850) and L7-GFP (004690).

Retro-orbital injections. AAV was diluted to 200 µl in 0.9% NaCl (Fresenius Kabi; 918610) before injection. Anaesthesia was induced with 4% isoflurane. Following induction, as measured by unresponsiveness to a toe pinch, the right eye was protruded by gentle pressure on the skin, and a tuberculin syringe was advanced, with the bevel facing away from the eye, into the retrobulbar sinus where AAV mix was slowly injected. For assessments of CNS editing, 1×10^{11} vg GFP–KASH virus was added to the injection mix as a transduction marker. Genomic DNA was purified from minced tissue using Agencourt DNAdvance kits (Beckman Coulter; A48705) in accordance with the manufacturer's instructions.

P0 ventricle injections. Drummond PCR pipettes (5-000-1001-X10) were pulled at the ramp test value on a Sutter P1000 micropipette puller and passed through a Kimwipe three times, resulting in a tip size of ~100 µm. A small amount of Fast Green was added to the AAV injection solution to assess ventricle targeting. The injection solution was loaded via front filling using the included Drummond plungers. P0 pups were anaesthetized by placement on ice for 2–3 min until they were immobile and unresponsive to a toe pinch. Then, 2 µl of injection mix was injected freehand into each ventricle. Ventricle targeting was assessed by the spread of Fast Green throughout the ventricles via transillumination of the head.

Nuclear isolation and sorting. Cerebella were separated from the brain with surgical scissors, hemispheres were separated using a scalpel, and the hippocampus and neocortex were separated from underlying midbrain tissue with a curved spatula. Nuclei were isolated from brain tissue as previously described[78]. All steps were performed on ice or at 4 °C. Dissected tissue was homogenized using a glass dounce homogenizer (Sigma–Aldrich; D8938; 20 strokes with pestle A followed by 20 strokes with pestle B) in 2 ml of ice-cold EZ-PREP buffer (Sigma–Aldrich; NUC-101). Samples were incubated for 5 min with an additional 2 ml EZ-PREP buffer. Nuclei were centrifuged at 500*g* for 5 min and the supernatant was removed. Samples were resuspended with gentle pipetting in 4 ml of ice-cold Nuclei Suspension Buffer consisting of 100 µg ml^{-1} BSA and 3.33 µM Vybrant DyeCycle Violet (Thermo Fisher Scientific) in 1× PBS, and centrifuged at 500*g* for 5 min. The supernatant was removed and nuclei were resuspended in 1–2 ml Nuclei Suspension Buffer, passed through a 35-µm strainer, and sorted into 200-µl Agencourt DNAdvance lysis buffer using a MoFlo Astrios (Beckman Coulter) at the Broad Institute flow cytometry core. Genomic DNA was purified according to the Agencourt DNAdvance instructions for a volume of 200 µl.

P14 sub-retinal injections. Each 1 µl of AAV mix for sub-retinal injections consisted of 4×10^9 vg of each split CBE base-editor half and 2×10^9 vg GFP for the PHP.B variant. The Anc80 + CBE3.9max mixture was divided equally: 3.3×10^8 vg of each split base-editor half and 3.3×10^8 vg GFP. The Anc80 + ABEmax mixture consisted of 4.5×10^8 vg of each split base-editor half and 4.5×10^8 vg GFP. PHP.B or Anc80 GFP alone at 5×10^9 vg μl^{-1} was injected into wild-type C57BL/6 mice to assess the transduction efficiency. P14 mice were anaesthetized by intraperitoneal injection of ketamine (140 mg kg^{-1}) and xylazine (14 mg kg^{-1}). Using a microscope for visualization, a small incision was made at the limbus using a 30-gauge needle, and a Hamilton syringe with a 33-gauge blunt-ended needle was used to inject 1 µl of AAV mix. Following injection, mice were placed on a 37 °C warming pad until they recovered.

Retina dissociation and cell sorting. Three weeks post-injection, eyes were enucleated and stored in BGJB medium (Thermo Fisher Scientific) on ice, as described previously[79]. Retinas were isolated under a fluorescent dissection microscope to record the transfected region, and dissociated into single cells by incubation in solution A containing 1 mg ml^{-1} pronase (Sigma–Aldrich) and 2 mM EGTA in BGJB medium at 37 °C for 20 min. Solution A was gently removed, followed by the addition of an equal amount of solution B containing 100 U ml^{-1} DNase I (New England Biolabs), 0.5% BSA and 2 mM EGTA in BGJB medium. Cells were collected and resuspended in 1× PBS, filtered through a cell strainer (BD Biosciences), and sorted using a FACSAria II (BD Biosciences).

Retinal histology. Mice injected with PHP.B or Anc80 GFP alone were sacrificed 3 weeks post-injection and perfused with 4% paraformaldehyde in 1× PBS. Eyes were dissected and eye cups were embedded in OCT freezing medium. Retinal cryosections were cut to 10 µm and stained with 4,6-diamidino-2-phenylindole (DAPI). Images were taken using an Eclipse Ti microscope (Nikon).

Brain immunohistochemistry. For comparison of PRE sequences, mice were transcardially perfused with PBS followed by 4% PFA. Harvested brains were rotated in 4% paraformaldehyde (PFA) at 4 °C overnight for post-fixation. Brains were transferred to 30% sucrose in 1× PBS for cryoprotection and rotated at 4 °C until equilibrated, as assessed by loss of buoyancy. Cryoprotected brains were frozen in a dry ice–ethanol bath and sectioned horizontally on a Leica CM1950 at 20 µm. For analysis of Purkinje neurons and activated microglia, brains were dissected and drop-fixed in 4% PFA overnight on a rotator. Brains were transferred to 1× PBS with 10 mM glycine and rotated at 4 °C for at least 24 h. Slices were embedded in 3% agarose for sagittal sectioning on a Leica VT1200 at 20 µm. Midline saggital slices were taken by mounting the agarose blocks containing individual hemispheres on the lateral surface. Only 50 sections were taken to minimize regional variability across animals. For each marker, three to ten slices per animal were analysed. The immunostaining procedure was identical for both cases: samples were blocked and permeabilized in 3% BSA (Jackson ImmunoResearch) and 0.1% Trition-X 100 in PBS. Samples were incubated in primary antibody at 4 °C overnight, washed three times for 10 min each with PBS containing 0.1% Triton-X (PBSTx), incubated with secondary antibody at room temperature for 1 h, washed 3× for 10 min with PBSTx, and mounted in ProLong Diamond Antifade with DAPI (Thermo Fisher Scientific). In some cases, slides were mounted in ProLong Diamond Antifade (without DAPI) supplemented with 5 µM DRAQ5 (a far-red DNA stain) to label DNA. Slides were cured overnight at room temperature before imaging. Care was taken to minimize light exposure at all steps. The primary antibodies used were as follows: chicken anti-GFP (10 µg ml^{-1}; Abcam; ab13970); rabbit anti-RFP (1.6 µg ml^{-1}; Rockland; 600-401-379); rabbit anti-Calbindin (0.1 µg ml^{-1}; Cell Signaling Technology; D1I4Q); rat anti-CD68 (1 µg ml^{-1}; Bio-Rad MCA1957); and mouse anti-Cas9 (5 µg ml^{-1}; Clone 7A9; Thermo Fisher Scientific; MA5-23519). Alexa-conjugated goat secondary antibodies (Thermo Fisher Scientific) were used at 1:500. Calbindin was imaged using Alexa 647-conjugated secondary antibodies to avoid bleedthrough from virally delivered GFP. Images were captured and stitched at 10× magnification using a Zeiss Axio Scan.Z1 and the included software. Image intensity was kept below 50% saturation to prevent oversaturation.

Image analysis. Images were analysed using ImageJ (Fiji), ilastik[80] and CellProfiler[81]. Details and custom ImageJ macros are provided in the Supplementary Methods. A subset of images were manually analysed by a blinded experimenter to validate the accuracy of the final imaging pipelines. Differences between the automated and manual counts were <10%.

Off-target analysis. CIRCLE-Seq was performed as previously described[82]. PCR amplification before sequencing was conducted using PhusionU polymerase, and products were gel-purified and quantified with a KAPA library quantification kit before loading onto an Illumina MiSeq. Data was processed using the CIRCLE-Seq analysis pipeline with the following parameters: 'read_threshold: 4; window_size: 3; mapq_threshold: 50; start_threshold: 1; gap_threshold: 3; mismatch_threshold: 6; merged_analysis: True'. The three sites found by CIRCLE-Seq analysis were chosen for PCR amplification and high-throughput sequencing. CRISPOR analysis[83] was done and the top five off-target candidates by cutting frequently determination score were analysed by amplicon sequencing.

***Npc1*^{I1061T} survival measurements.** *Npc1*^{I1061T} mice were euthanized at the onset of morbidity, which was defined functionally as profound ataxia leading to an inability to acquire food and water, as evidenced by a low body condition score[84,85] and minimal responsiveness to touch. In all cases, a low body condition score

preceded profound ataxia. Profound ataxia was the diagnostic criterion for morbundity. The end point was designed to minimize suffering while providing accurate survival data. Euthanasia recommendations were made by a blinded veterinary technician. All survival groups were mixed sex.

Statistical analysis. Unpaired two-sided *t*-tests were used to compare the immunofluorescence datasets. The log-rank (Mantel–Cox) test was used to compare Kaplan–Meier survival curves. All statistical tests were calculated using GraphPad. No corrections were made for multiple comparisons.

Reporting Summary. Further information on research design is available in the Nature Research Reporting Summary linked to this article.

Data availability

The data that support the results of this study are available within the paper and its Supplementary Information. All unmodified reads for sequencing-based data in the manuscript are available from the NCBI Sequence Read Archive under accession number PRJNA532891. AAV genome sequences are provided in the Supplementary Information. Key plasmids from this work will be available from Addgene (depositor: D.R.L.), and other plasmids and raw data are available from the corresponding author on request.

Code availability

The custom code used in this study is provided in the Supplementary Information.

Received: 20 June 2019; Accepted: 4 December 2019;
Published online: 14 January 2020

References

1. Landrum, M. J. et al. ClinVar: public archive of relationships among sequence variation and human phenotype. *Nucleic Acids Res.* **42**, D980–D985 (2014).
2. Rees, H. A. & Liu, D. R. Base editing: precision chemistry on the genome and transcriptome of living cells. *Nat. Rev. Genet.* **19**, 770–788 (2018).
3. Komor, A. C., Kim, Y. B., Packer, M. S., Zuris, J. A. & Liu, D. R. Programmable editing of a target base in genomic DNA without double-stranded DNA cleavage. *Nature* **533**, 420–424 (2016).
4. Gaudelli, N. M. et al. Programmable base editing of A•T to G•C in genomic DNA without DNA cleavage. *Nature* **551**, 464–471 (2017).
5. Komor, A. C. et al. Improved base excision repair inhibition and bacteriophage Mu Gam protein yields C:G-to-T:A base editors with higher efficiency and product purity. *Sci. Adv.* **3**, eaao4774 (2017).
6. Koblan, L. W. et al. Improving cytidine and adenine base editors by expression optimization and ancestral reconstruction. *Nat. Biotechnol.* **36**, 843–846 (2018).
7. Nishida, K. et al. Targeted nucleotide editing using hybrid prokaryotic and vertebrate adaptive immune systems. *Science* **353**, aaf8729 (2016).
8. Ryu, S. M. et al. Adenine base editing in mouse embryos and an adult mouse model of Duchenne muscular dystrophy. *Nat. Biotechnol.* **36**, 536–539 (2018).
9. Yeh, W. H., Chiang, H., Rees, H. A., Edge, A. S. B. & Liu, D. R. In vivo base editing of post-mitotic sensory cells. *Nat. Commun.* **9**, 2184 (2018).
10. Chadwick, A. C., Wang, X. & Musunuru, K. In vivo base editing of PCSK9 (proprotein convertase subtilisin/kexin type 9) as a therapeutic alternative to genome editing. *Arterioscl. Thromb. Vas.* **37**, 1741–1747 (2017).
11. Russell, S. et al. Efficacy and safety of voretigene neparvovec (AAV2-hRPE65v2) in patients with *RPE65*-mediated inherited retinal dystrophy: a randomised, controlled, open-label, phase 3 trial. *Lancet* **390**, 849–860 (2017).
12. Carvalho, L. S. et al. Evaluating efficiencies of dual AAV approaches for retinal targeting. *Front. Neurosci.* **11**, 503 (2017).
13. Wu, Z., Yang, H. & Colosi, P. Effect of genome size on AAV vector packaging. *Mol. Ther.* **18**, 80–86 (2010).
14. Liu, D. R., Levy, J, M. & Yeh, W. H. AAV delivery of nucleobase editors. US patent 15/784,033 (2017).
15. Truong, D. J. J. et al. Development of an intein-mediated split-Cas9 system for gene therapy. *Nucleic Acids Res.* **43**, 6450–6458 (2015).
16. Zetsche, B., Volz, S. E. & Zhang, F. A split-Cas9 architecture for inducible genome editing and transcription modulation. *Nat. Biotechnol.* **33**, 139–142 (2015).
17. Wright, A. V. et al. Rational design of a split-Cas9 enzyme complex. *Proc. Natl Acad. Sci. USA* **112**, 2984–2989 (2015).
18. Zettler, J., Schutz, V. & Mootz, H. D. The naturally split Npu DnaE intein exhibits an extraordinarily high rate in the protein *trans*-splicing reaction. *FEBS Lett.* **583**, 909–914 (2009).
19. Davis, K. M., Pattanayak, V., Thompson, D. B., Zuris, J. A. & Liu, D. R. Small molecule-triggered Cas9 protein with improved genome-editing specificity. *Nat. Chem. Biol.* **11**, 316–318 (2015).
20. Stevens, A. J. et al. Design of a split intein with exceptional protein splicing activity. *J. Am. Chem. Soc.* **138**, 2162–2165 (2016).
21. Shah, N. H., Eryilmaz, E., Cowburn, D. & Muir, T. W. Extein residues play an intimate role in the rate-limiting step of protein *trans*-splicing. *J. Am. Chem. Soc.* **135**, 5839–5847 (2013).
22. Swiech, L. et al. In vivo interrogation of gene function in the mammalian brain using CRISPR–Cas9. *Nat. Biotechnol.* **33**, 102–106 (2015).
23. Kim, Y. B. et al. Increasing the genome-targeting scope and precision of base editing with engineered Cas9-cytidine deaminase fusions. *Nat. Biotechnol.* **35**, 371–376 (2017).
24. Villiger, L. et al. Treatment of a metabolic liver disease by in vivo genome base editing in adult mice. *Nat. Med.* **24**, 1519–1525 (2018).
25. Grieger, J. C. & Samulski, R. J. Packaging capacity of adeno-associated virus serotypes: impact of larger genomes on infectivity and postentry steps. *J. Virol.* **79**, 9933–9944 (2005).
26. Deverman, B. E. et al. Cre-dependent selection yields AAV variants for widespread gene transfer to the adult brain. *Nat. Biotechnol.* **34**, 204–209 (2016).
27. Choi, J. H. et al. Optimization of AAV expression cassettes to improve packaging capacity and transgene expression in neurons. *Mol. Brain* **7**, 17 (2014).
28. Zuris, J. A. et al. Cationic lipid-mediated delivery of proteins enables efficient protein-based genome editing in vitro and in vivo. *Nat. Biotechnol.* **33**, 73–80 (2015).
29. Rees, H. A. et al. Improving the DNA specificity and applicability of base editing through protein engineering and protein delivery. *Nat. Commun.* **8**, 15790 (2017).
30. Gray, S. J. et al. Optimizing promoters for recombinant adeno-associated virus-mediated gene expression in the peripheral and central nervous system using self-complementary vectors. *Hum. Gene Ther.* **22**, 1143–1153 (2011).
31. Ran, F. A. et al. In vivo genome editing using *Staphylococcus aureus* Cas9. *Nature* **520**, 186–191 (2015).
32. Mendell, J. R. et al. Single-dose gene-replacement therapy for spinal muscular atrophy. *N. Engl. J. Med.* **377**, 1713–1722 (2017).
33. Wu, Z., Asokan, A. & Samulski, R. J. Adeno-associated virus serotypes: vector toolkit for human gene therapy. *Mol. Ther.* **14**, 316–327 (2006).
34. Duan, D. Systemic AAV micro-dystrophin gene therapy for Duchenne muscular dystrophy. *Mol. Ther.* **26**, 2337–2356 (2018).
35. Garvilles, R. G. et al. Dual functions of the RFTS domain of Dnmt1 in replication-coupled DNA methylation and in protection of the genome from aberrant methylation. *PLoS ONE* **10**, e0137509 (2015).
36. Feng, J. et al. Dnmt1 and Dnmt3a maintain DNA methylation and regulate synaptic function in adult forebrain neurons. *Nat. Neurosci.* **13**, 423–430 (2010).
37. Inagaki, K. et al. Robust systemic transduction with AAV9 vectors in mice: efficient global cardiac gene transfer superior to that of AAV8. *Mol. Ther.* **14**, 45–53 (2006).
38. Duan, D., Yue, Y. & Engelhardt, J. F. Expanding AAV packaging capacity with *trans*-splicing or overlapping vectors: a quantitative comparison. *Mol. Ther.* **4**, 383–391 (2001).
39. Xu, Z. et al. *Trans*-splicing adeno-associated viral vector-mediated gene therapy is limited by the accumulation of spliced mRNA but not by dual vector coinfection efficiency. *Hum. Gene Ther.* **15**, 896–905 (2004).
40. Van Putten, M. et al. Low dystrophin levels increase survival and improve muscle pathology and function in dystrophin/utrophin double-knockout mice. *FASEB J.* **27**, 2484–2495 (2013).
41. Li, D., Yue, Y. & Duan, D. Marginal level dystrophin expression improves clinical outcome in a strain of dystrophin/utrophin double knockout mice. *PLoS ONE* **5**, e15286 (2010).
42. Tuchman, M., Jaleel, N., Morizono, H., Sheehy, L. & Lynch, M. G. Mutations and polymorphisms in the human ornithine transcarbamylase gene. *Hum. Mutat.* **19**, 93–107 (2002).
43. Treacy, E. P. et al. Analysis of phenylalanine hydroxylase genotypes and hyperphenylalaninemia phenotypes using L-[1-^{13}C]phenylalanine oxidation rates in vivo: a pilot study1. *Pediatr. Res.* **42**, 430–435 (1997).
44. Hamman, K. et al. Low therapeutic threshold for hepatocyte replacement in murine phenylketonuria. *Mol. Ther.* **12**, 337–344 (2005).
45. Zincarelli, C., Soltys, S., Rengo, G. & Rabinowitz, J. E. Analysis of AAV serotypes 1–9 mediated gene expression and tropism in mice after systemic injection. *Mol. Ther.* **16**, 1073–1080 (2008).
46. Asico, L. D. et al. Nephron segment-specific gene expression using AAV vectors. *Biochem. Biophys. Res. Commun.* **497**, 19–24 (2018).
47. Foust, K. D. et al. Intravascular AAV9 preferentially targets neonatal neurons and adult astrocytes. *Nat. Biotechnol.* **27**, 59–65 (2009).
48. Mercuri, E. et al. Nusinersen versus sham control in later-onset spinal muscular atrophy. *N. Engl. J. Med.* **378**, 625–635 (2018).
49. Chan, K. Y. et al. Engineered AAVs for efficient noninvasive gene delivery to the central and peripheral nervous systems. *Nat. Neurosci.* **20**, 1172–1179 (2017).
50. Hordeaux, J. et al. The neurotropic properties of AAV-PHP.B are limited to C57BL/6J mice. *Mol. Ther.* **26**, 664–668 (2018).

51. Huang, Q. et al. Delivering genes across the blood-brain barrier: LY6A, a novel cellular receptor for AAV-PHP.B capsids. *PLoS ONE* **14**, e0225206 (2019).
52. Harvey, R. J. & Napper, R. M. Quantitative study of granule and Purkinje cells in the cerebellar cortex of the rat. *J. Comp. Neurol.* **274**, 151–157 (1988).
53. Vogel, M. W., Sunter, K. & Herrup, K. Numerical matching between granule and Purkinje cells in lurcher chimeric mice: a hypothesis for the trophic rescue of granule cells from target-related cell death. *J. Neurosci.* **9**, 3454–3462 (1989).
54. Kim, J. Y. et al. Viral transduction of the neonatal brain delivers controllable genetic mosaicism for visualising and manipulating neuronal circuits in vivo. *Eur. J. Neurosci.* **37**, 1203–1220 (2013).
55. Kim, J. Y., Grunke, S. D., Levites, Y., Golde, T. E. & Jankowsky, J. L. Intracerebroventricular viral injection of the neonatal mouse brain for persistent and widespread neuronal transduction. *J. Vis. Exp.* **91**, 51863 (2014).
56. Hoxha, E., Balbo, I., Miniaci, M. C. & Tempia, F. Purkinje cell signaling deficits in animal models of ataxia. *Front. Syn. Neurosci.* **10**, 6 (2018).
57. Matilla-Duenas, A. et al. Consensus paper: pathological mechanisms underlying neurodegeneration in spinocerebellar ataxias. *Cerebellum* **13**, 269–302 (2014).
58. Chakrabarty, P. et al. Capsid serotype and timing of injection determines AAV transduction in the neonatal mice brain. *PLoS ONE* **8**, e67680 (2013).
59. Madisen, L. et al. A robust and high-throughput Cre reporting and characterization system for the whole mouse brain. *Nat. Neurosci.* **13**, 133–140 (2010).
60. Zinn, E. et al. In silico reconstruction of the viral evolutionary lineage yields a potent gene therapy vector. *Cell Rep.* **12**, 1056–1068 (2015).
61. Koch, S. F. et al. Genetic rescue models refute nonautonomous rod cell death in retinitis pigmentosa. *Proc. Natl Acad. Sci. USA* **114**, 5259–5264 (2017).
62. Maeder, M. L. et al. Development of a gene-editing approach to restore vision loss in Leber congenital amaurosis type 10. *Nat. Med.* **25**, 229–233 (2019).
63. Park, W. D. et al. Identification of 58 novel mutations in Niemann–Pick disease type C: correlation with biochemical phenotype and importance of PTC1-like domains in NPC1. *Hum. Mutat.* **22**, 313–325 (2003).
64. Praggastis, M. et al. A murine Niemann–Pick C1 I1061T knock-in model recapitulates the pathological features of the most prevalent human disease allele. *J. Neurosci.* **35**, 8091–8106 (2015).
65. Yu, T., Shakkottai, V. G., Chung, C. & Lieberman, A. P. Temporal and cell-specific deletion establishes that neuronal Npc1 deficiency is sufficient to mediate neurodegeneration. *Hum. Mol. Genet.* **20**, 4440–4451 (2011).
66. Loftus, S. K. et al. Rescue of neurodegeneration in Niemann–Pick C mice by a prion-promoter-driven Npc1 cDNA transgene. *Hum. Mol. Genet.* **11**, 3107–3114 (2002).
67. Lopez, M. E., Klein, A. D., Dimbil, U. J. & Scott, M. P. Anatomically defined neuron-based rescue of neurodegenerative Niemann–Pick type C disorder. *J. Neurosci.* **31**, 4367–4378 (2011).
68. Elrick, M. J. et al. Conditional Niemann–Pick C mice demonstrate cell autonomous Purkinje cell neurodegeneration. *Hum. Mol. Genet.* **19**, 837–847 (2010).
69. Ko, D. C. et al. Cell-autonomous death of cerebellar Purkinje neurons with autophagy in Niemann–Pick type C disease. *PLoS Genet.* **1**, 81–95 (2005).
70. Langmade, S. J. et al. Pregnane X receptor (PXR) activation: a mechanism for neuroprotection in a mouse model of Niemann–Pick C disease. *Proc. Natl Acad. Sci. USA* **103**, 13807–13812 (2006).
71. Hughes, M. P. et al. AAV9 intracerebroventricular gene therapy improves lifespan, locomotor function and pathology in a mouse model of Niemann–Pick type C1 disease. *Hum. Mol. Genet.* **27**, 3079–3098 (2018).
72. Ling, C. et al. High-efficiency transduction of primary human hematopoietic stem/progenitor cells by AAV6 vectors: strategies for overcoming donor-variation and implications in genome editing. *Sci. Rep.* **6**, 35495 (2016).
73. Nathwani, A. C. et al. Long-term safety and efficacy of factor IX gene therapy in hemophilia B. *N. Engl. J. Med.* **371**, 1994–2004 (2014).
74. Chandler, R. J. et al. Systemic AAV9 gene therapy improves the lifespan of mice with Niemann–Pick disease, type C1. *Hum. Mol. Genet* **26**, 52–64 (2017).
75. Xie, C., Gong, X. M., Luo, J., Li, B. L. & Song, B. L. AAV9-NPC1 significantly ameliorates Purkinje cell death and behavioral abnormalities in mouse NPC disease. *J. Lipid Res.* **58**, 512–518 (2017).
76. Hinderer, C. et al. Severe toxicity in nonhuman primates and piglets following high-dose intravenous administration of an adeno-associated virus vector expressing human SMN. *Hum. Gene Ther.* **29**, 285–298 (2018).
77. Manno, C. S. et al. Successful transduction of liver in hemophilia by AAV-factor IX and limitations imposed by the host immune response. *Nat. Med.* **12**, 342–347 (2006).
78. Habib, N. et al. Massively parallel single-nucleus RNA-Seq with DroNc-Seq. *Nat. Methods* **14**, 955–958 (2017).
79. Li, P. et al. Allele-specific CRISPR–Cas9 genome editing of the single-base P23H mutation for rhodopsin-associated dominant retinitis pigmentosa. *CRISPR J.* **1**, 55–64 (2018).
80. Sommer, C., Strähle, C., Köthe, U. & Hamprecht, F. A. Ilastik: Interactive learning and segmentation toolkit. In *Eighth IEEE International Symposium on Biomedical Imaging* 230–233 (ISBI, 2011).
81. Carpenter, A. E. et al. CellProfiler: image analysis software for identifying and quantifying cell phenotypes. *Genome Biol.* **7**, R100 (2006).
82. Tsai, S. Q. et al. CIRCLE-Seq: a highly sensitive in vitro screen for genome-wide CRISPR–Cas9 nuclease off-targets. *Nat. Methods* **14**, 607–614 (2017).
83. Haeussler, M. et al. Evaluation of off-target and on-target scoring algorithms and integration into the guide RNA selection tool CRISPOR. *Genome Biol.* **17**, 148 (2016).
84. Ullman-Cullere, M. H. & Foltz, C. J. Body condition scoring: a rapid and accurate method for assessing health status in mice. *Lab. Anim. Sci.* **49**, 319–323 (1999).
85. Foltz, C. & Ullman-Cullere, M. Guidelines for assessing the health and condition of mice. *Lab Animal* **28**, 28–32 (1998).

Acknowledgements

This work was supported by the US National Institutes of Health (grant nos. UG3 TR002636, U01 AI142756, RM1 HG009490, R01 EB022376 and R35 GM118062), St. Jude Collaborative Research Consortium, DARPA (HR0011-17-2-0049), Ono Pharma Foundation, Bill and Melinda Gates Foundation and Howard Hughes Medical Institute. We thank the Harvard Center for Biological Imaging for infrastructure and support. We thank F. Zhang, B. Deverman and K. Chan for equipment access, guidance and helpful discussions, M. Doan for image analysis assistance and A. Hamidi for assistance with editing the manuscript.

Author contributions

J.M.L. designed the research, constructed the plasmids, produced the AAV and performed the HEK cell, mouse systemic and CNS injection experiments. W.-H.Y. performed all of the CBE 3T3 experiments, image analysis and off-target analysis. J.R.D. performed the ABE 3T3 experiments. L.W.K. constructed the plasmids and performed the HEK cell experiments. N.P., R.B. and E.H. performed the retinal experiments. J.C. conceived of the retinal experiments and performed the data analysis. Q.L. conceived of and performed the sub-retinal injection experiments and data analysis. D.R.L. designed and supervised the research. J.M.L., W.-H.Y. and D.R.L. wrote the manuscript. All authors contributed to editing the manuscript.

Competing interests

D.R.L. is a consultant and co-founder of Beam Therapeutics, Prime Medicine, Editas Medicine and Pairwise Plants, all of which are companies that use genome editing. D.R.L., J.M.L., W.-H.Y. and L.W.K. have filed patent applications on AAV systems for base editor delivery. The remaining authors declare no competing interests.

Additional information

Supplementary information is available for this paper at https://doi.org/10.1038/s41551-019-0501-5.

Correspondence and requests for materials should be addressed to D.R.L.

Reprints and permissions information is available at www.nature.com/reprints.

Publisher's note Springer Nature remains neutral with regard to jurisdictional claims in published maps and institutional affiliations.

nature research

Corresponding author(s): David R. Liu

Last updated by author(s): Dec 1, 2019

Reporting Summary

Nature Research wishes to improve the reproducibility of the work that we publish. This form provides structure for consistency and transparency in reporting. For further information on Nature Research policies, see Authors & Referees and the Editorial Policy Checklist.

Statistics

For all statistical analyses, confirm that the following items are present in the figure legend, table legend, main text, or Methods section.

n/a	Confirmed	
☐	☒	The exact sample size (*n*) for each experimental group/condition, given as a discrete number and unit of measurement
☐	☒	A statement on whether measurements were taken from distinct samples or whether the same sample was measured repeatedly
☐	☒	The statistical test(s) used AND whether they are one- or two-sided *Only common tests should be described solely by name; describe more complex techniques in the Methods section.*
☒	☐	A description of all covariates tested
☒	☐	A description of any assumptions or corrections, such as tests of normality and adjustment for multiple comparisons
☐	☒	A full description of the statistical parameters including central tendency (e.g. means) or other basic estimates (e.g. regression coefficient) AND variation (e.g. standard deviation) or associated estimates of uncertainty (e.g. confidence intervals)
☐	☒	For null hypothesis testing, the test statistic (e.g. *F*, *t*, *r*) with confidence intervals, effect sizes, degrees of freedom and *P* value noted *Give P values as exact values whenever suitable.*
☒	☐	For Bayesian analysis, information on the choice of priors and Markov chain Monte Carlo settings
☒	☐	For hierarchical and complex designs, identification of the appropriate level for tests and full reporting of outcomes
☒	☐	Estimates of effect sizes (e.g. Cohen's *d*, Pearson's *r*), indicating how they were calculated

Our web collection on statistics for biologists contains articles on many of the points above.

Software and code

Policy information about availability of computer code

Data collection	HTS data, images, and flow-cytometry data were collected with standard commerical llumina MiSeq, Zeiss Axio Scan, and Beckman Astrios/BD FACSDiva software, respectively.
Data analysis	HTS data were analyzed by CRISPResso2. Images were analyzed by custom ImageJ (v. 1.52p) macros and Cell Profiler 3.1.9/ilastik 1.3.3, as described in the Supplementary Information.

For manuscripts utilizing custom algorithms or software that are central to the research but not yet described in published literature, software must be made available to editors/reviewers. We strongly encourage code deposition in a community repository (e.g. GitHub). See the Nature Research guidelines for submitting code & software for further information.

Data

Policy information about availability of data

All manuscripts must include a data availability statement. This statement should provide the following information, where applicable:

- Accession codes, unique identifiers, or web links for publicly available datasets
- A list of figures that have associated raw data
- A description of any restrictions on data availability

The data supporting the results in this study are available within the paper and its Supplementary Information. All unmodified reads for sequencing-based data in the manuscript are available from the NCBI Sequence Read Archive, under accession number PRJNA532891. AAV genome sequences are provided in the Supplementary Information. Key plasmids from this work will be available from Addgene (depositor: David R. Liu), and other plasmids and raw data are available from the corresponding author on request.

Field-specific reporting

Please select the one below that is the best fit for your research. If you are not sure, read the appropriate sections before making your selection.

☒ Life sciences ☐ Behavioural & social sciences ☐ Ecological, evolutionary & environmental sciences

For a reference copy of the document with all sections, see nature.com/documents/nr-reporting-summary-flat.pdf

Life sciences study design

All studies must disclose on these points even when the disclosure is negative.

Sample size	Sample sizes were chosen in accord with the standards of the field, which have historically been sufficient for the development and validation of genome-editing tools.
Data exclusions	A single eye was removed from the subretinal injection experiment (Fig. 5) after no GFP-positive cells were observed. A single retro-orbital injection was removed from the terminator optimization experiment after no GFP-positive cells were observed (Fig. 2a - 2c). These events are likely the result of failed injections, or arose from other technical issues that would prevent proper analysis. These exclusion criteria were not formally established before the start of data collection.
Replication	Independent replicates are all reported. All attempts at reproducibility succeeded, as defined by (at a minimum) two or three positive results.
Randomization	NPC1 mice were assigned to the treated or untreated groups by litter. No covariates were controlled.
Blinding	Image-analysis pipelines were generated by a blinded experimenter. NPC1 euthanasia recommendations were made by a blinded investigator. All HTS data was analysed by an unblinded operator by using an automated CRISPResso2 script with limited experimenter intervention.

Reporting for specific materials, systems and methods

We require information from authors about some types of materials, experimental systems and methods used in many studies. Here, indicate whether each material, system or method listed is relevant to your study. If you are not sure if a list item applies to your research, read the appropriate section before selecting a response.

Materials & experimental systems

n/a	Involved in the study
☐	☒ Antibodies
☐	☒ Eukaryotic cell lines
☒	☐ Palaeontology
☐	☒ Animals and other organisms
☒	☐ Human research participants
☒	☐ Clinical data

Methods

n/a	Involved in the study
☒	☐ ChIP-seq
☐	☒ Flow cytometry
☒	☐ MRI-based neuroimaging

Antibodies

Antibodies used	Immunofluorescence: Primary: chicken polyclonal anti-GFP, 10 µg/mL (1:1000, Abcam ab13970); rabbit polyclonal anti-RFP, 1.6 µg/mL (1:1000, Rockland 600-401-379); rabbit monoclonal clone D1I4Q anti-Calbindin, 0.1 µg/mL. (1:500, Cell Signaling Technology 13176, lot 3); rat monoclonal anti-CD68 clone FA-11, 1 µg/mL (1:1000, Bio-Rad MCA1957); mouse monoclonal anti-Cas9 clone 7A9, 5 µg/ml (1:500, Thermo Fisher MA5-23519). Secondary: Thermo Fisher Goat anti-Chicken IgY (H+L) Secondary Antibody, Alexa Fluor 488 A-11039 Thermo Fisher Goat anti-Rabbit IgG (H+L) Highly Cross-Adsorbed, Alexa Fluor 488 A-11034 Thermo Fisher Goat anti-Rabbit IgG (H+L) Secondary Antibody, Alexa Fluor 555 A-21428 Thermo Fisher Goat anti-Rabbit IgG (H+L) Highly Cross-Adsorbed, Alexa Fluor Plus 647 A-32733 Westerns: Primary antibodies used were rabbit monoclonal anti-GAPDH clone D16H11, 1:1000 (Cell Signaling Technologies 5174), rabbit monoclonal anti-HA, clone C29F4, 1:1000 (Cell Signaling Technologies 3724), mouse monoclonal anti-FLAG, clone M2, 1 µg/mL (Sigma F1804). LI-COR IRDye 680RD goat anti-rabbit (#926-68071) and goat anti-mouse (#926-68070) secondary antibodies were used at 1:10,000-1:20,000 dilutions.
Validation	Each antibody was validated for species and application, as appropriate, on the manufacturer's website, as supported by the relevant citations on the product pages. FLAG and HA antibodies were validated in-house with GFP-transfected and untransfected controls.

Eukaryotic cell lines

Policy information about cell lines

Cell line source(s)	HEK293T and NIH 3T3 cells were obtained from ATCC.
Authentication	None of the cell lines were authenticated.
Mycoplasma contamination	All cells initially tested negative for mycoplasma by the manufacturer. Cells were periodically tested during experimentation. No mycoplasma contamination was found.
Commonly misidentified lines (See ICLAC register)	No commonly misidentified cell lines were used.

Animals and other organisms

Policy information about studies involving animals; ARRIVE guidelines recommended for reporting animal research

Laboratory animals	Wild-type mus musculus C57BL/6NCrl and C57BL/6J. Npc1tm(I1061T)Dso (C57BL/6J background; JAX #027704); Ai9 (C57BL/6J; #007909); Rhodopsin-iCre (C57BL/6 x SJL; #015850); L7-GFP (FVB/N; #004690). Males and females were used in equal proportions. Animals were aged from P0 to P110.
Wild animals	The study did not involve wild animals.
Field-collected samples	The study did not involve samples collected from the field.
Ethics oversight	The Broad Institute and Massachusetts Eye and Ear IACUCs provided ethical approval for animal experiments.

Note that full information on the approval of the study protocol must also be provided in the manuscript.

Flow Cytometry

Plots

Confirm that:

☒ The axis labels state the marker and fluorochrome used (e.g. CD4-FITC).

☒ The axis scales are clearly visible. Include numbers along axes only for bottom left plot of group (a 'group' is an analysis of identical markers).

☒ All plots are contour plots with outliers or pseudocolor plots.

☒ A numerical value for number of cells or percentage (with statistics) is provided.

Methodology

Sample preparation	For nuclei sorting: Nuclei were harvested from mouse brains for sorting: Cerebella were separated from the brain with surgical scissors, hemispheres were separated using a scalpel, and the hippocampus and neocortex were separated from underlying midbrain tissue with a curved spatula. All subsequent steps were performed on ice or at 4 °C. Dissected tissue was homogenized using a glass dounce homogenizer (Sigma D8938) (20 strokes with pestle A followed by 20 strokes with pestle B) in 2 mL ice-cold EZ-PREP buffer (Sigma NUC-101). Samples were incubated for 5 minutes with an additional 2 mL EZ-PREP buffer. Nuclei were centrifuged at 500 g for 5 minutes, and the supernatant removed. Samples were resuspended with gentle pipetting in 4 mL ice-cold Nuclei Suspension Buffer (NSB) consisting of 100 µg/mL BSA and 3.33 µM Vybrant DyeCycle Violet (Thermo Fisher) in 1xPBS, and centrifuged at 500 g for 5 minutes. The supernatant was removed and nuclei were resuspended in 1-2 mL NSB, passed through a 35 µm strainer, and kept on ice for sorting. For retinal sorting: Eyes were enucleated and stored in BGJB medium on ice. Retinas were isolated under a fluorescent dissection microscope to record the transfected region and dissociated into single cells by incubation in solution A containing 1 mg/mL pronase and 2 mM EGTA in BGJB medium at 37 °C for 20 minutes. Solution A was gently removed, followed by adding equal amount of solution B containing 100 U/mL DNase I, 0.5% BSA, 2 mM EGTA in BGJB medium. Cells were collected and re-suspended in 1xPBS, filtered through a cell strainer (BD Biosciences) and kept on ice for sorting.
Instrument	Brain: MoFlo Astrios EQ (Beckman Coulter); retina: FACSAriaII (BD Biosciences)
Software	Brain: Data were collected using Summit 6.3.1 and analyzed using FlowJo 10.2. Retina: data were analyzed using BD FACSDiva 8.0.1 software
Cell population abundance	GFP and/or tdTomato-positive populations were checked for purity by re-running an aliquot of sorted cells on several occasions. >99% of sorted cells were GFP-positive.
Gating strategy	Brain: DAPI-positive events were collected and back-gated to establish FSC/SSC gates. SSC height/SSC width was used to select single events. GFP-positive events were clearly separated from GFP-negative events; initial experiments used a GFP-negative

control to define populations.
Retina: Debris was gated out using SSC-A vs. FSC-A graph. FSC-W vs. FSC-A and SSC-W vs. SSC-A graphs were used to select single events. GFP only, tdTomato only, double positive, and double negative cells were isolated and collected based on clear populations in the tdTomato vs. GFP graph.

☒ Tick this box to confirm that a figure exemplifying the gating strategy is provided in the Supplementary Information.